1

2

The impact of coregistration of gradient recalled echo images on quantitative susceptibility and R2* mapping at 7T

5

6 Seongjin Choi[1], Xu Li[2,3], and Daniel M. Harrison[1]

7

8 [1]Department of Neurology, University of Maryland School of Medicine, Baltimore,

9 Maryland, United Stated of America

10 [2]F.M. Kirby Research Center for Functional Brain Imaging, Kennedy Krieger Institute,

11 Baltimore, Maryland, United Stated of America

12 [3]Department of Radiology and Radiological Science, Johns Hopkins University School

13 of Medicine, Baltimore, Maryland, United States of America

14

15 *Corresponding author: Seongjin Choi

16 E-mail: seongjin.choi@som.umaryland.edu (SC)

17

20 **Short title:** Impact of co-registration approaches on QSM and R2*

21

22

23

Abstract

Introduction: While image coregistration is inevitable and quantitative parametric maps, such as R2* and QSM, are increasingly used in multi-parametric studies of the brain, there is a lack of investigations on the reliability of quantitative metrics after coregistration. The purposes of this study were 1) to evaluate the reliability of R2* and QSM at 7T and 2) to assess the statistical agreement in the quantitative metrics obtained by two different coregistration approaches.

Methods: We compared the reliability of R2* and quantitative susceptibility maps obtained from brains of eight healthy participants by two coregistration approaches: 1) transformation of pre-processed quantitative maps and 2) processing quantitative maps after transformation using pixel- and ROI-based analyses. Two-sample Kolmogorov-Smirnov, Mann-Whitney U, Paired T, Intraclass-correlation tests were performed appropriately.

Results: R2* remained invariant regardless of the cogeneration timing. However, magnetic susceptibility was significantly altered when processed in transformed space, whereas it remained invariant in all KS-tests and pixel values were only different in 2 out of 64 U-tests for direct QSM coregistration. Paired t-test revealed that ROI-based group-mean R2* was invariant to both approaches, while group-mean susceptibility was invariant to direct coregistration but differed in one structure processed in transformed space. For all pairs of measurements of R2*, ICCs were excellent. ICCs for magnetic susceptibility were excellent when processed in its native space while the ICCs were lower than 0.9 or poor when processed in transformed space. Further analysis revealed that the choice of interpolation approach affected the resultant QSM.

47 **Conclusions:** Our study shows that R2* could be safely processed in a transformed

48 space, whereas QSM was less reliable when processed in the transformed space.

49 Hence, caution is advised when using QSM in a multi-parametric study, and it is

50 strongly recommended to process QSM in its native space prior to any coregistration or

51 spatial transformation.

52

53

Introduction

54

55   Image coregistration is an inevitable step of data processing in contemporary

56 studies using magnetic resonance imaging (MRI) data because of increasing demands

57 for multi-parametric image analyses. Further, combined quantitative image analysis

58 often requires coregistration of several MR images of various spatial resolutions as well

59 as different contrasts into a common image space. Image coregistration is also

60 essential in longitudinal studies, in which MR images are acquired and accumulated

61 across a few time points.

62

63   Image coregistration often employs multiple sophisticated mathematical

64 algorithms, for example, geometric transformation, interpolation, and estimation of pixel

65 values (PVs) from a source image in a transformed space. Hence, in the transformed

66 space, the resulting image may consist of voxels of altered spatial locations,

67 dimensions, and intensity values compared to the original image. Therefore, some

68 researchers may raise concerns about the reliability of metrics derived from the altered

69 PVs in the transformed space.

70

71   Although individual PVs of the coregistered image in a transformed space may

72 be altered, data derived from a post-registration image may still be useful for multi-

73 parametric analyses if the descriptive statistics and the distribution profile of the PVs in

74 structural labels or regions of interest (ROI) remain statistically identical. If the statistical

75 features of altered PVs in the transformed space are significantly different from those of

76 its source MR image, any metrics derived from the transformed image are not reliable

77 and should not be considered in further analysis.

78

79   While image coregistration is inevitable and various quantitative parametric

80 maps, such as R2* and quantitative susceptibility mapping (QSM), are increasingly

81 used in studies employing multiparametric assessment of the brain, there is a lack of

82 investigations on the reliability of the derived quantitative metrics after source image

83 coregistration. There are a limited number of studies investigating the reproducibility of

84 QSM. [1-4] Hinoda et al. assessed the consistency and reproducibility of QSM at 3T and

85 1.5T and demonstrated good reproducibility of QSM processed by two different

86 background phase removal algorithms at both field strengths. [1] Deh et al. assessed

87 the reproducibility of nonlinear MEDI-based QSM measurements in both control and

88 patient groups for scanners from two different vendors and at both 3T and 1.5T. Their

89 QSM measurements showed good intra-scanner and inter-scanner reproducibility for

90 healthy and multiple sclerosis participants. [2] Santin et al. investigated the

91 reproducibility of QSM measurements at 3T in healthy volunteers within and between

92 different MR sessions using four different combinations of QSM reconstruction methods.

4

93 [3] They also investigated the reproducibility of R2* measurements in comparison with

94 QSM measurements. Lauzon et al. compared QSM acquired by various methodologies.

95 [4] They showed that readout gradient polarity and accelerated parallel imaging did not

96 alter the estimated susceptibility at 3T. In summary, these studies reported inter-vendor,

97 inter-acquisition methods, inter/intra-scanner, inter-field (1.5 and 3T), and inter-QSM

98 reconstruction methods agreements. More recently, a few more studies explored QSM

99 reliability or reproducibility at ultra-high field (7T). Lancione et al. demonstrated excellent

100 intra-scanner repeatability and inter-scanner reproducibility of QSM at both 3T and 7T

101 within five healthy subjects of mixed gender. [5] Rua et al. investigated the

102 reproducibility of QSM and R2* map at 7T and showed promising results for multi-center

103 and multi-vendor planforms within three healthy male subjects. [6] Okada et al.

104 investigated test-retest reliability of cortical R2* and QSM at 7T within sixteen healthy

105 subject and both measures showed repeatable results in the wide cortical area except

106 at the frontal-temporal base area. [7]

107

108 However, none of these studies investigated the impact of co-registration of

109 source gradient recalled echo (GRE) images to a non-native space on the resulting

110 parametric maps of R2* and quantitative susceptibility. In these studies, when inter-

111 space coregistrations were required, the resultant quantitative maps were coregistered

112 after being processed in their native spaces, although there has been no empirical

113 evidence to do so. Moreover, reliabilities of QSM and R2* maps have not been fully

114 explored at ultra-high field (7T). In this study, we investigated the influence of two

115 different coregistration approaches on quantitative measurements (R2* and magnetic

5

116 susceptibility) acquired at 7T in particular. We examined the reliability of quantitative

117 measures collected within four atlas-based structural labels in deep brain areas

118 bilaterally using both pixel- and ROI-based analyses. We addressed how two

119 coregistration approaches differently impact on R2* map and QSM. Furthermore, we

120 addressed how an insignificant modification of phase-image resolution led to a

121 significant change in resultant QSM.

122

123

Materials and Methods

125 This study consists of two stages. Initial stage was performed to assess the

126 reliability of 7T R2* and QSM and impact of the coregistration approaches. Then, based

127 on the initial analysis results, a further analysis was conducted to address the questions

128 raised in the initial analysis.

129

Participants

131 Eight healthy subjects with ages ranging from 32 to 57 (four men, four women)

132 participated in the study. The Institutional Review Boards at the Johns Hopkins

133 University School of Medicine and the Kennedy Krieger Institute approved protocols,

134 and all participants provided written informed consent.

135

Acquisition

137 MRI was acquired using a whole-body 7T Achieva MR scanner (Philips Medical

138 Systems, Cleveland, OH, USA) and a volume-transmit, 32-channel receive head coil

139 (Nova Medical, Wilmington, MA, USA). MRI protocol consisted of a magnetization

140 prepared rapid acquisition gradient echo sequence (MPRAGE, TR/TE = 4.1/1.83 ms,

141 sagittal acquisition, FOV = 180 × 220 × 220 mm^3, image matrix = 180 × 220 × 220, flip

142 angle = 7 degrees, TFE factor = 352, SENSE factor = 2 × 1 × 2) and a multi-echo 3D

143 gradient-recalled echo sequence (GRE, TR/TE1/ΔTE = 68/4/2 ms, 8 echoes, axial

144 acquisition, FOV = 220 × 220 × 110 mm^3, image matrix = 224 × 224 × 110) with both

145 magnitude and phase output.

146

Image processing

Preprocessing

149   All pre- and post-processing steps were performed on a Linux (Debian 8)

150 desktop with Neurodebian packages [8]. Before starting any image processing, all MRI

151 data saved in Par/Rec format (Philips native format) were converted to NIfTI format

152 using the 'parrec2nii' module in 'NIPY' package written in Python script language [9].

153 MPRAGE data were corrected for the bias field using the N4 bias-field correction

154 algorithm prior to linear registration [10]. Then, linear coregistration of GRE data to

155 MPRAGE space was performed using FLIRT (FMRIB, Oxford University) with rigid body

156 transformation [11, 12]. A transformation matrix (GRE-to-MPRAGE transformation

157 matrix) was acquired for coregistration of the first-echo magnitude image of GRE to

158 MPRAGE space. The first-echo magnitude was chosen because it has the least signal

159 loss due to intra-voxel spin dephasing and ensures preserving the most brain tissues.

160 For calculating QSM in MPRAGE space, magnitude and phase image pairs were then

161 converted to real and imaginary pairs using FSLUTILS included in FSL. The

162 transformation matrix was then applied to the real and imaginary image pairs. Finally,

163 the transformed real and imaginary pair was converted back to a magnitude and phase

164 image pair for further processing in MPRAGE space. The QSM processing in a

165 transformed space requires consideration of its dependency on coregistration

166 transformation matrix. Hence, we assured use of a transformed dipole kernel in QSM

167 processing in MPRAGE space by reflecting angle changes introduced by transformation

168 matrix from GRE to MRPAGE spaces.

169

170 **R2* mapping**

171   Two sets of R2* maps were calculated in a voxel-wise manner using the power

172 method, in which the decay of squared magnitudes from all eight echoes was fitted to a

173 monoexponential model. [13] This was performed using an in-house tool written in

174 MatLab (Mathworks, Inc., Natick, MA). One set of R2* maps was calculated in its native

175 (GRE) space, and another set was calculated from GRE data transformed to MPRAGE

176 space. The third set of R2* maps was acquired by direct transformation of the R2* map

177 in its native space to MPRAGE space using the GRE-to-MPRAGE transformation matrix

178 acquired during preprocessing.

179

180 **Quantitative Susceptibility Mapping (QSM)**

181   Three sets of QSM data were also calculated for each participant. The first two

182 sets of QSMs were processed using GRE images in native space and GRE images

183 transformed to MPRAGE space. Although QSM can be calculated from both single-

8

184　echo and multi-echo GRE data [14], we only processed multi-echo QSM. QSM

185　processing was accomplished using an in-house tool (JHU QSM Toolbox) written in

186　Matlab. The first three echoes (at TE of 4 ms, 6 ms, and 8 ms) were excluded from

187　calculating QSM to avoid non-linear temporal phase evolution in white matter when TE

188　is shorter than 10 ms at ultra-high field [15, 16], and the other five echoes (with TE of 10

189　ms to 18 ms) underwent the phase processing and were averaged to generate the final

190　frequency map and susceptibility maps. Phase images underwent a sequential process

191　of phase unwrapping, background-field removal, and dipole inversion. Phase

192　unwrapping employed a Laplacian-based phase unwrapping algorithm [17]. The

193　unwrapped phase images were then divided by 2π*TE to obtain an image of frequency

194　shift in Hz. Background field removal was peformed by the V-SHARP method [18-20]

195　with a maximum spherical kernel size of 6 mm and TSVD threshold of 0.05. Then,

196　dipole inversion was performed by applying a modified structural feature based

197　collaborative reconstruction (SFCR) algorithm with only L1-norm based regularization

198　i.e. $\lambda_1 = \gamma_1 = 100$ and dropped L2-norm regularization i.e. $\lambda_2 = \gamma_2 = 0$ [21]. Finally, the

199　last set of QSM was acquired by directly coregistering QSM in native (GRE) space to

200　MPRAGE space using the GRE-to-MPRAGE transformation matrix saved in

201　preprocessing.

202

Structural label preparation and data collection

204　　Two sets of structural labels in MPRAGE and GRE spaces for each participant

205　were prepared. Atlas-based structural labels were used to avoid biases introduced by

206　manual drawing. We used structural labels obtained from the Harvard-Oxford atlas,

9

207 which is included in FSL and based on T1-weighted images of 37 healthy subjects of

208 mixed genders in standard MNI 152 space. The source atlas contained labels for each

209 structure bilaterally. Four anatomical structures from this atlas were bilaterally selected

210 for analysis: thalamus (TH_L and TH_R), caudate nucleus (CN_L and CN_R), globus

211 pallidus (GP_L and GP_R), and putamen (PUT_L and PUT_R). Using FSL, the atlas-

212 based labels were eroded by one voxel (with 3-D kernel) to ensure that measurements

213 were performed only within the intended structures after the following image

214 transformations and to reduce potential partial volume effect between other structures

215 and other tissue types in the vicinity. The eroded structural labels were then inversely

216 warped to the MPRAGE space of each participant using FNIRT available in FSL

217 (FMRIB, Oxford University) [22]. These labels were used to collect PVs from parametric

218 maps in MPRAGE space. Finally, the labels were linearly transformed to each

219 participant's GRE space with the inverse of the GRE-to-MPRAGE transformation matrix.

220 These labels were used to collect PVs from parametric maps in GRE space. Using the

221 two sets of labels in GRE and MPRAGE spaces, we sampled voxel-based data for the

222 selected four structures bilaterally. These pixel-based data were further used to

223 calculate group-mean values for each structural label. Fig 1 shows the eight structures

224 in the standard (MNI), GRE, and MPRAGE spaces of a representative participant.

225

226 **Fig 1. Example of structural labels in a representative participant.**

227 Axial (top row) and coronal (bottom row) views of four bilateral (thus 8) structural labels

228 in three spaces: MNI (left), MPRAGE (center), and GRE (right) spaces. Caudate

229 nucleus (red, CN), putamen (green, PUT), globus pallidus (purple, GP), and thalamus

230 (blue, TH) were bilaterally segmented using the Harvard-Oxford Atlas available in FSL.

231 Colored structures are the results of erosion of the source structures (white) using one-

232 voxel sized 3-D kernel.

233

Data analysis

235 All statistical analyses and data visualization were carried out using R software

236 package (R Core team, Vienna, Austria). P-values less than 0.05 were considered as

237 significant for all analyses. Adjustments for multiple comparisons were not performed

238 due to the small sample size and exploratory nature of this study.

239

Pixel-based analysis

241 We assessed the reliability of quantitative R2* and QSM metrics processed and

242 collected in transformed space versus those processed in native space but collected in

243 transformed space by comparing PV distributions and PV similarity in reference to

244 metrics from R2* and QSM processed and collected in native space.

245

246 Since all sampled data violated the assumption of normal distribution, non-

247 parametric methods were employed to evaluate the reliability of PVs. We selected the

248 'Two-sample Kolmogorov-Smirnov test (KS-test)' to assess the distribution equality of

249 two compared data sets. The result of KS test is the D-statistic, which quantifies a

250 distance between empirical distribution functions of the two compared data sets. We

251 also used the 'Man-Whitney U-test (U-test)' to check differences between two compared

252 data sets.

253

Region-of-Interest (ROI) based analysis

255 The purpose of this analysis was to investigate ROI-based group mean

256 comparison. This type of comparison is usually performed to detect statistical difference

257 between two groups, e.g. patient group versus controls. In our study, we applied this

258 analysis to examine the reliability of group mean (of all subjects) of R2* and magnetic

259 susceptibility values in eight structures. The mean values of R2* and QSM for each

260 structure were calculated using PVs from the pixel-based analysis. We performed a

261 qualitative review of mean metrics using bar plots. The 'Paired t-test' was used to

262 assess the reliability of the mean metrics before and after linear coregistration.

263

264 In addition to the paired t-test, we also conducted intra-class correlation (ICC)

265 test. ICC estimates and their 95% confidence intervals were calculated based on single

266 measurement, absolute agreement, and two-way mixed effects model using 'irr'

267 package available for R. The purpose of this ICC analysis was to assess the agreement

268 between mean quantitative metrics for each structure acquired in GRE and MPRAGE

269 spaces across all subjects.

270

Further analysis on the impact of interpolating source GRE on resultant QSM

273 Noticing that coregistration included interpolation of images during alignment of

274 two images, we investigated the impact of the interpolation of the source GRE image on

275 the resultant QSM by interpolating GRE image to the resolution of MPRAGE image.

12

276 Another QSM was then processed in GRE space by directly interpolating to the

277 MRPAGE space resolution for comparison. The QSM results, which were processed in

278 its native GRE and an interpolated GRE spaces, were examined by comparing images,

279 density plots and distance measured by D-statistic from KS-test. Further, we attempted

280 observing the error propagation along the QSM processing chain.

281

282

283 # Results

284 ## Pixel-based analysis

285 R2* maps were robust to both coregistration approaches. Fig 2 visualizes KS-test

286 results by comparing the empirical cumulative distribution function (ECDF) of R2* maps.

287 KS- and U-test results comparing PVs of R2* maps showed no significant difference

288 caused by either GRE to MPRAGE coregistration (D-statistic ranged from 0.008670 to

289 0.03769, U-statistic ranged from 94387 to 16655829, all $p > 0.05$) or direct R2*

290 coregistration to MPRAGE space (D-statistic ranged from 0.007509 to 0.4770, all $p >$

291 0.05, U-statistic ranged from 94889 to 16684842, all $p > 0.05$). Complete tables for KS-

292 and U-tests results for R2* metrics is provided in S1 and S2 Tables.

293

294 **Fig 2. Empirical cumulative distribution functions (ECDF) of R2* maps acquired**

295 **using two different coregistration approaches in a representative participant.**

296 (a) ECDF's of R2* pixel values acquired from its native GRE space (red) and from GRE

297 data transformed to MPRAGE space (cyan) were overlaid. In this approach, R2*

298 calculation was performed after the coregistration of GRE data to MPRAGE space. (b)

13

299 ECDFs of R2* pixel values acquired from its native GRE space (red) and from R2* map

300 directly coregistered to MPRAGE space (cyan) were overlaid. In this approach, R2*

301 map calculation is performed in its native space and, then, the resultant R2* map is

302 coregistered to MPRAGE space. All ECDFs showed excellent agreement for the

303 distributions of PVs. Similar results were confirmed in all participants. Regardless of the

304 differences in processing steps, ECDF's from both methods are well overlapped without

305 significant differences in R2* values.

306

307   Fig 3 (a) visualizes discrepancies found between PV distributions of QSMs

308 processed in GRE and in MPRAGE spaces as poorly matched ECDFs. KS-tests

309 detected differences in 61 out of 64 structures (8 structural labels x 8 participants). U-

310 tests found differences in 55 out of 64 structures. A full result is provided in S3 Table.

311 On the other hand, Fig 3 (b) visualizes good agreement between QSMs processed in

312 GRE space and directly coregistered to MPRAGE space. KS-tests detected differences

313 in only 1 out of 64 structures. U-tests found differences in only 1 out of 64 structures. A

314 full table of the results is provided in S4 Table. Our KS- and U-test results showed that

315 susceptibility measurements were significantly altered in most structures of all

316 participants after the coregistration of GRE images to MPRAGE space. In general,

317 these results indicate that linear coregistration of the source GRE images significantly

318 altered the distribution and PVs of the resultant QSM, while direct coregistration of QSM

319 to a reference space did not alter the distributions and PVs.

320

321 **Fig 3. Empirical cumulative distribution functions (ECDF) of QSM by two different**

322 **coregistration approaches.**

323 (a) ECDFs of magnetic susceptibility pixel values acquired from its native GRE space

324 (red) and from GRE data transformed to MPRAGE space (cyan) were overlaid. In this

325 approach, QSM calculation was performed after the coregistration of GRE data to

326 MPRAGE space. (b) ECDFs of magnetic susceptibility pixel values acquired from QSM

327 in GRE space (red) and the QSM directly coregistered to MPRAGE space (cyan) were

328 overlaid. In this approach, QSM calculation was performed first and, then, the QSM was

329 coregistered to MPRAGE space. Significant discrepancies were observed between

330 QSM in GRE and MPRAGE spaces when the source GRE was transformed to

331 MPRAGE space prior to QSM processing. On the contrary, the QSM-calculation-then-

332 coregistration approach did not show significant differences in the pixel-based analysis

333 except in one structure in one participant

334

335   Further analysis of frequency maps in an effort to investigate the discrepancy

336 between QSMs acquired by two coregistration approaches was performed. Figure 4

337 shows one of the results in a representative participant. Noticeable differences were

338 observed in 6 out of 8 structures between frequency maps processed in GRE and

339 MPRAGE spaces respectively. ECDFs of frequency maps of Left and right putamen

340 (PUT_L and PUT_R) did not show apparent discrepancies in this specific case. The

341 differences between frequency maps did not result in a predictable matter in QSMs.

342 Instead, corresponding QSM in PUT_L and PUT_R were significantly different between

15

343   spaces where QSMs were processed as seen in Fig 3 (a). A full table of this analysis is

344   provides in S5 Table.

345

346   **Fig 4. Empirical cumulative distribution functions (ECDF) of frequency maps by**

347   **two different coregistration approaches.**

348   ECDFs in 8 structural labels of frequency map acquired after coregistration of source

349   GRE data to MPRAGE space (cyan) as compared to the corresponding frequency and

350   QSM in its native GRE space (red) in a representative participant. Relatively better

351   overlapped ECDFs in PUT_L and PUT_R of frequency maps did not lead to better

352   overlapped ECDFs of QSM, which still showed significant differences in the two

353   structures as seen in Fig 3 (a).

354

Region-of-Interest (ROI) based analysis

356   The paired t-test was conducted on the paired group-mean measurement, which

357   is the mean (8 subjects) of means (intra-structure). The group-mean measurements of

358    $R2^*$ were statistically equivalent ($p > 0.05$ for all structures) as shown in Table 1 and 2.

359   Fig 5 shows group-mean measurements of $R2^*$ within each structure of all participants

360   for both coregistration approaches. This indicates that group-mean $R2^*$ is reliable to

361   either coregistration of GRE data to MPRAGE space (Fig 5 (a)) or its direct

362   coregistration to MPRAGE space (Fig 5 (b)) in all structures.

363

364   **Fig 5. Comparison of group-mean $R2^*$ acquired by two different coregistration**

365   **approaches.**

16

366 R2* was robust to either coregistration of source GRE data to MPRAGE space (a) or its

367 direct coregistration to MPRAGE space (b) in all structures. See also Tables 1 and 2.

368 (TH_L: left thalamus, TH_R: right thalamus, CN_L: left caudate nucleus, CN_R: right

369 caudate nucleus, GP_L: left globus pallidus, GP_R: right globus pallidus, PUT_L: left

370 putamen, PUT_R: right putamen)

371

372

373 **Table 1. Mean R2* (in the unit of Hz) comparison by paired T-test for**

374 **coregistration of source GRE data to MRPAGE space before R2* calculation.**

structure	mean R2* (SD) in GRE space	mean R2* (SD) in MPRAGE space	P-value (CI)
CN_L	46.4 (5.22)	46.4 (5.24)	0.154 (-0.118, 0.0229)
CN_R	44.5 (4.07)	44.6 (4.09)	0.776 (-0.168, 0.13)
GP_L	87.8 (13.9)	87.9 (13.7)	0.679 (-0.494, 0.341)
GP_R	87 (16.2)	87.1 (16.1)	0.385 (-0.284, 0.124)
PUT_L	53.3 (7.68)	53.3 (7.6)	0.678 (-0.267, 0.185)
PUT_R	55.7 (9.79)	55.7 (9.86)	0.747 (-0.143, 0.19)
TH_L	39.5 (3.05)	39.6 (3.04)	0.164 (-0.0995, 0.0205)
TH_R	40.6 (4.92)	40.6 (4.96)	0.596 (-0.0434, 0.07)

375

376 SD: Standard deviation, CI: Confidence interval

377 CN_L: left caudate nucleus, CN_R: right caudate nucleus, GP_L: left globus pallidus,

378 GP_R: right globus pallidus, PUT_L: left putamen, PUT_R: right putamen, TH_L: left

379 thalamus, TH_R: right thalamus

380

381

17

382 **Table 2. Mean R2* (in the unit of Hz) comparison by paired T-test for direct**

383 **coregistration of R2* map in GRE space to MPRAGE space.**

structure	mean R2* (SD) in GRE space	mean R2* (SD) in MPRAGE space	P-value (CI)
CN_L	46.4 (5.22)	46.4 (5.25)	0.59 (-0.0925, 0.0568)
CN_R	44.5 (4.07)	44.5 (4.09)	0.991 (-0.117, 0.116)
GP_L	87.8 (13.9)	88 (13.8)	0.406 (-0.52, 0.237)
GP_R	87 (16.2)	87.1 (16.1)	0.913 (-0.254, 0.231)
PUT_L	53.3 (7.68)	53.3 (7.55)	0.543 (-0.255, 0.147)
PUT_R	55.7 (9.79)	55.7 (9.89)	0.563 (-0.146, 0.247)
TH_L	39.5 (3.05)	39.6 (3.02)	0.155 (-0.0656, 0.0127)
TH_R	40.6 (4.92)	40.5 (4.96)	0.208 (-0.0321, 0.123)

384

385 SD: Standard deviation, CI: Confidence interval

386 CN_L: left caudate nucleus, CN_R: right caudate nucleus, GP_L: left globus pallidus,

387 GP_R: right globus pallidus, PUT_L: left putamen, PUT_R: right putamen, TH_L: left

388 thalamus, TH_R: right thalamus

389

390 The group-means of magnetic susceptibilities showed better reliability than pixel-based

391 analyses as shown in Tables 3 and 4. Fig 6 shows comparisons of group-mean

392 measurements of magnetic susceptibility. The results show good statistical equivalence

393 in most structures when processed in transformed space or direct coregistration of

394 QSMs.

395

396 **Table 3. Mean magnetic susceptibility (in the unit of ppm) comparison by paired**

397 **T-test for coregistration of source GRE data to MRPAGE space before QSM**

398 **processing.**

Structure	mean χ_m (SD) in GRE space	mean χ_m (SD) in MPRAGE space	P-value (CI)
CN_L	0.0527 (0.02)	0.0454 (0.0239)	0.117 (-0.00234, 0.0168)
CN_R	0.0448 (0.0155)	0.0453 (0.0241)	0.906 (-0.0108, 0.00975)
GP_L	0.135 (0.0238)	0.127 (0.0294)	0.141 (-0.00362, 0.0206)
GP_R	0.119 (0.039)	0.108 (0.0447)	0.147 (-0.00491, 0.0268)
PUT_L	0.0519 (0.00817)	0.0481 (0.0121)	0.177 (-0.00217, 0.00976)
PUT_R	0.062 (0.0167)	0.0557 (0.017)	< 0.05 (0.00213, 0.0105)
TH_L	-0.00625 (0.00787)	0.00292 (0.0147)	0.0758 (-0.0196, 0.00124)
TH_R	-0.00489 (0.00992)	0.00285 (0.0131)	0.0775 (-0.0166, 0.00111)

399

400   χ_m: magnetic susceptibility

401   SD: Standard deviation, CI: Confidence interval

402   CN_L: left caudate nucleus, CN_R: right caudate nucleus, GP_L: left globus pallidus,

403   GP_R: right globus pallidus, PUT_L: left putamen, PUT_R: right putamen, TH_L: left

404   thalamus, TH_R: right thalamus

405

406   **Table 4. Mean magnetic susceptibility (in the unit of ppm) comparison by paired**

407   **T-test for direct coregistration of QSM in GRE space to MPRAGE space.**

structure	mean χ_m (SD) in GRE space	mean χ_m (SD) in MPRAGE space	P-value (CI)
CN_L	0.0527 (0.02)	0.0526 (0.02)	0.776 (-0.000201, 0.000258)
CN_R	0.0448 (0.0155)	0.0448 (0.0155)	0.760 (-0.000189, 0.000145)
GP_L	0.135 (0.0238)	0.135 (0.0234)	0.622 (-0.00077, 0.000495)
GP_R	0.119 (0.039)	0.119 (0.0394)	0.722 (-0.00107, 0.00147)
PUT_L	0.0519 (0.00817)	0.0522 (0.00772)	0.585 (-0.00132, 0.000809)
PUT_R	0.062 (0.0167)	0.0616 (0.0171)	0.325 (-0.000465, 0.00122)
TH_L	-0.00625 (0.00787)	-0.00627 (0.00791)	0.537 (-0.0000547,0.0000961)
TH_R	-0.00489 (0.00992)	-0.00492 (0.00991)	0.480 (-0.0000733, 0.000141)

408   χ_m: magnetic susceptibility

409   SD: Standard deviation, CI: Confidence interval

410   CN_L: left caudate nucleus, CN_R: right caudate nucleus, GP_L: left globus pallidus,

411   GP_R: right globus pallidus, PUT_L: left putamen, PUT_R: right putamen, TH_L: left

412   thalamus, TH_R: right thalamus

413

414   **Fig 6. Comparison of group-mean magnetic susceptibilities acquired by two**

415   **different coregistration approaches.**

416   (a) Comparison of QSM values in its native space (red) and in MPRAGE space (cyan)

417   obtained by coregistration of source GRE data. Although differences are noticeable in

418   group-mean susceptibility they are statistically significant except for one label (PUT_R).

419   (b) QSM was robust to its direct coregistration to MPRAGE space in all structures. The

420   group-mean susceptibilities were almost identical in GRE and MPRAGE spaces when

421   QSM was directly coregistered. Therefore, coregistration of resultant QSM to a target

422   space would be a better reproducible approach in most brain structures. (TH_L: left

423   thalamus, TH_R: right thalamus, CN_L: left caudate nucleus, CN_R: right caudate

424   nucleus, GP_L: left globus pallidus, GP_R: right globus pallidus, PUT_L: left putamen,

425   PUT_R: right putamen)

426

427   The intra-class correlation coefficient (ICC) was conducted on the mean (intra-

428   structure) measurement. For all pairs of measurements of R2*, the estimated ICCs were

429   higher than 0.9 as shown in Table 5. For magnetic susceptibility, ICCs were higher than

430   0.9 between the measurements processed in GRE space and those directly

20

431 transformed to MPRAGE space. ICCs were between 0.75 and 0.9 in five out of eight

432 structures between the magnetic susceptibilities estimated in GRE space and the ones

433 in transformed space and three structures showed ICCs between 0.5 and 0.75 or lower

434 than 0.5.

435

436 **Table 5. Intraclass correlation (ICC) coefficients.**

structure	R2* (GRE vs. MPRAGE)		R2* (GRE vs direct coreg.)		χ_m (GRE vs. MPRAGE)		χ_m (GRE vs direct coreg.)	
	ICC (CI)	P_value	ICC (CI)	P_value	ICC (CI)	P_value	ICC (CI)	P_value
CN_L	1 (0.999, 1)	<0.001	1 (0.999, 1)	<0.001	0.834 (0.38, 0.964)	<0.05	1 (1, 1)	<0.001
CN_R	0.999 (0.996, 1)	<0.001	0.999 (0.997, 1)	<0.001	0.834 (0.357, 0.965)	<0.05	1 (1, 1)	<0.001
GP_L	0.999 (0.997, 1)	<0.001	0.999 (0.998, 1)	<0.001	0.826 (0.378, 0.962)	<0.05	1 (0.998, 1)	<0.001
GP_R	1 (0.999, 1)	<0.001	1 (0.999, 1)	<0.001	0.879 (0.523, 0.974)	<0.001	0.999 (0.997, 1)	<0.001
PUT_L	0.999 (0.997, 1)	<0.001	1 (0.998, 1)	<0.001	0.734 (0.194, 0.939)	<0.05	0.988 (0.945, 0.998)	<0.001
PUT_R	1 (0.999, 1)	<0.001	1 (0.999, 1)	<0.001	0.897 (0.146, 0.982)	<0.05	0.998 (0.992, 1)	<0.001
TH_L	1 (0.998, 1)	<0.001	1 (0.999, 1)	<0.001	0.357 (-0.2, 0.807)	0.114	1 (1, 1)	<0.001
TH_R	1 (1, 1)	<0.001	1 (0.999, 1)	<0.001	0.501 (-0.107, 0.867)	0.0536	1 (1, 1)	<0.001

437

438 R2* is in the unit of Hz

439 χ_m: magnetic susceptibility in ppm

440 CI: confidence interval

441 CN_L: left caudate nucleus, CN_R: right caudate nucleus, GP_L: left globus pallidus,

442 GP_R: right globus pallidus, PUT_L: left putamen, PUT_R: right putamen, TH_L: left

443 thalamus, TH_R: right thalamus

444

445 **Impact of coregistration of source GRE on resultant QSM**

446 **Impact of interpolation**

21

447   Interpolation to different image resolution did not change magnitude or raw phase

448   images visually as in Fig 7. While interpolated QSM after processing did not show

449   significant differences (KS-test, D = 0.00175, p > 0.05) from the QSM in native space,

450   QSM calculated from magnitude and phase images interpolated to different spatial

451   resolution showed significant differences (D = 0.00992, p < 0.001) as in Fig 8.

452

453   **Fig 7. No significant impact of interpolation on raw images.**

454   Interpolation did not change the source image drastically: (a) magnitude image in GRE

455   space (0.982x0.982 mm^2), (b) phase image in GRE space, (c) magnitude image

456   interpolated to MPRAGE space resolution (1x1 mm^2 in plane resolution), (d) phase

457   image interpolated to MPRAGE space resolution.

458

459   **Fig 8. Impact of two interpolation approaches on QSM.**

460   QSM directly interpolated was not significantly different from QSM processed in its

461   native space (a) and (b). On the contrary, source GRE interpolation resulted in

462   significantly different QSM distributions (c) and (d).

463

464   **Impact of coregistration on each step of QSM calculation chain**

465   Coregistration, which included not only interpolation but also angle changes

466   between GRE and MPRAGE space, also did not cause significant statistical difference

467   (D = 0.000639, p = 0.977) between raw phase distributions of GRE and interpolated

468   GRE images (Fig 9 (a)). However, when they were unwrapped, distribution was (D =

469   0.268, p < 0.001) significantly different (Fig 9 (b)). This difference was reflected on

22

470 frequency maps (D = 0.00659, p < 0.001) (Fig 9 (c)) and eventually caused significant

471 difference (D = 0.0212, p < 0.001) between resultant QSMs. (Fig 9 (d)) QSM from

472 source GRE coregistration was different than source GRE interpolation from the QSM in

473 native space.

474

475 **Fig 9. Small error in source GRE coregistration propagates along the QSM**

476 **processing chain.**

477 Although coregistration did not cause statistical differences in raw phase images (a),

478 when it was unwrapped differences were distinguishable (b). This caused differences in

479 frequency maps and eventually caused differences in QSM (d). Phase images of 4-th

480 echo out of 5 echoes used to calculate the frequency map and QSM are shown here.

481

482

Discussion

Reliability of R2* and QSM at 7T

485   Our primary purpose was to evaluate the impact of linear coregistration methods

486 on GRE-derived metrics (R2* and QSM) acquired at 7T. Our results revealed that R2*

487 was a reliable metric when processed in either native GRE space or non-native

488 MPRAGE space, whereas magnetic susceptibility was not. The well-matched ECDFs

489 indicate that neither linear coregistration of GRE data nor direct coregistration of R2*

490 map to MRPAGE space alter the pixel values and distribution of R2* metrics. On the

491 contrary, ECDFs of QSM were only well matched for direct QSM registration to

492   MPRAGE space. This result implies that different approaches of coregistration may

493   affect the pixel values and distribution of resultant QSM significantly in different manner.

494   Therefore, QSM studies, in particular those employing pixel-based analysis, should be

495   limited to susceptibility values if QSMs are calculated in native space.

496

Difference between R2* and QSM processing

497

498   There are a number of possible reasons for the difference in the reliability of R2*

499   versus magnetic susceptibility found in this study. One source of this discrepancy may

500   arise from the intrinsically different characteristics of calculations used for R2* and

501   QSM. R2* is calculated only from the magnitude of GRE images, while QSM (V-SHARP

502   and SFCR in this study) utilizes mainly the phase. R2* calculated in a voxel-wise

503   manner is an inherently local entity, while QSM reconstruction involves complicated

504   dipole inversion that needs to take phase/frequency values in neighboring voxels into

505   account. Since R2* maps are calculated in a voxel-wise manner from magnitude

506   components across echo-times (TEs), any small magnitude difference within a voxel

507   stay local without propagation to other voxels. On the contrary, phase components are

508   determined by susceptibility sources not only within a voxel but also in surrounding and

509   remote voxels. Elkady et al.'s work demonstrated the requirement of an extended field-

510   of-view (5-fold) to minimize errors in QSM reconstruction of selected anatomical

511   structure. [23] From a different perspective, their work also suggests that any alteration

512   in QSM PV of a certain voxel could be caused by alterations in PVs of GRE

513   phase/frequency within surrounding or remote voxels even though the PV of

514   phase/frequency does not change in that voxel itself. This suspicion was to some extent

24

515 confirmed in that alteration patterns in PVs of frequency maps did not result in similar

516 alteration patterns in QSM PVs.

517

518 Another source of the discrepancy between our findings for R2* and QSM could be the

519 multiple-step nature of the QSM processing used in this study (phase unwrapping,

520 background phase removal, and dipole inversion, [24-26]), which may amplify the small

521 differences induced by coregistration. In order to minimize such error prorogations in

522 QSM processing, recently proposed single-step QSM methods would be preferred in

523 future studies. [27-29]

524

525 In our study, to ensure equivalent brain masks were used in both the native GRE

526 space and the MPRAGE spaces for background removal and QSM calculation, we used

527 the brain mask acquired in its native space, then, applied the GRE-to-MPRAGE

528 transformation matrix for the QSM reconstruction in the transformed space. However, if

529 the coregistration is not perfect with small discrepancies in the brain masks over the two

530 spaces, it could lead to differences in the estimated local frequency map during the

531 background field removal step (as in Figure 4) and further lead to discrepancies in the

532 final QSMs through the complicated dipole inversion step. Though the ill-posedness in

533 QSM dipole inversion [30, 31] could be overcome by applying the calculation of

534 susceptibility using multiple-orientation sampling (COSMOS), [32] only single orientation

535 data was acquired for the present study, and we had to use single-orientation QSM

536 method with regularization.

537

Difference in two coregistration approaches

538

539   There is an intrinsic difference between our two coregistration approaches with

540   previous works on reliability or reproducibility of R2* and QSM [1-4]. Previous works

541   compared two data of an identical image resolution. However, our reliability test was

542   performed for data sets of close but different image resolutions. From this perspective,

543   R2* calculation was not affected when it was processed with either native resolution or

544   non-native resolution. This indicates that a slight alteration of image resolution in a

545   transformed space does not affect resulting PVs or their distribution in R2* maps. On

546   the contrary, a similar reliability was not confirmed for QSM reconstruction in our study.

547

548   Previous studies have shown that direct coregistration of QSM was reliable for

549   various transformations including intra-individual coregistration [3] and spatial

550   normalization to MNI space. [1] Our study adds to this body of literature by providing

551   evidence of discrepancies introduced by processing QSM in a non-native space.

552   Collectively, these results suggest that QSM must be processed before coregistration of

553   its source GRE image to another image space. On the other hand, our results showed

554   statistical invariance of R2* metrics after the coregistration of GRE images at both pixel

555   and group levels. In these reliability tests, the agreement of R2* measurements before

556   and after coregistration suggest that R2* maps may serve as robust measurements

557   regardless of the timing of coregistration.

558

559   In contrast to the robustness of R2* metric to different coregistration approaches

560   at both pixel- and ROI-levels, differences observed in pixel-based analyses of QSM

26

561 measures were not statistically significant in ROI-based analyses when QSM was

562 processed in the transformed space. This is presumably due to the fact that individual

563 differences at the pixel level were averaged out for the ROIs. Although group mean

564 values of susceptibilities of most structures were statistically identical, noticeably bigger

565 differences were observed when QSM was processed in the transformed space as

566 compared to directly coregistered QSM values consistent with the pixel-value based

567 analysis. This result also suggests that ROI-based analysis and pixel-based analysis of

568 QSM may lead to contradictory conclusions – especially when QSM was derived from

569 transformed GRE data instead of its native space.

570

571 In addition, paired-t-test (for the paired χ_m mean of means) and ICC (for grouped

572 intra-structure means of χ_m) showed unreliability in different structures. This indicates

573 that a chosen statistical analysis approach may also affect the interpretation of a study

574 for group comparison when QSM is processed in a non-native space.

575

Impact of interpolation and coregistration

577 As an essential process in any coregistration, interpolation appeared to be a key

578 factor affecting the QSM result in a non-native space. It is closely related to what source

579 phase values are fed into the dipole inversion processing chain. Because of the ill-

580 posed nature of dipole inversion, slightly different source values as well as voxel counts

581 caused by altered voxel dimensions may lead to evidently different QSM after a long

582 chain calculation pipeline. Our results clearly showed how slightly different voxel

583 dimension of a source image could lead to distinguishable differences in resultant QSM.

584 Furthermore, these results suggest when large-scale cross-site data sets are compared,

585 it is critical to keep the image parameters as close as possible with extra care on source

586 image resolution in voxel based analyses.

587

588 **Limitations**

589 There are a few limitations in our study. Although our results showed excellent

590 statistical invariance of R2* to the linear coregistration of its source GRE image at the

591 pixel and group levels, the reliability of R2* for a non-linear transformation of the source

592 GRE images was not tested. Hence, our finding has to be limited to linear

593 coregistration. The robustness of statistical inference derived from R2* maps and QSMs

594 was not verified yet, and it is beyond the scope of this study. Our future work will include

595 the reliability of statistical relationships between quantitative metrics and clinical

596 measures under a similar coregistration of GRE images in a larger cohort including

597 control and patient groups. Further, our data were single-orientation QSM's. Therefore,

598 we could not verify if our results would apply for multi-orientation QSM, such as

599 COSMOS.[32] However, it has to be noticed that multi-orientation QSM increases total

600 scan time and, hence, is often impractical in a clinical study. [25] Furthermore, in our

601 study, QSM calibration to a reference region was not performed. Although QSM

602 calibration is being employed in recent QSM studies, there is no agreed reference

603 region for this referencing purpose.[1, 33-36] CSF has frequently been used for the

604 reference region in many studies.[33, 34] However, other regions have also been used.

605 [35] Some studies did not perform QSM calibration at all. [1, 36] There have also been

606 efforts to find suitable reference tissues for QSM. [35, 37] However, the selection of

607 reference region can be problematic when the region includes pathologic tissues.

608 Because we focused on the assessment of R2* maps and QSM before and after the

609 source GRE image coregistration in the context of reliability or reproducibility instead of

610 the accuracy of the metrics, analysis without QSM calibration to a reference region

611 should not undermine our study results. We did not conduct further analyses on

612 unwrapping, background removal and QSM reconstruction algorithms because it is

613 beyond the scope of our study.

614

615

Conclusions

617   To the best of our knowledge, the current study is the first report providing

618 quantitative analysis of the influence of source GRE image transformation on the

619 resultant parametric maps, R2* map and QSM in particular. Our study is in line with and

620 support prior reliability studies, but is distinguished from other work in that coregistration

621 was performed for not only resultant parametric maps but also source GRE images

622 providing complementary data which have not been explored before. In conclusion, R2*

623 maps are reliable when processed from GRE data linearly transformed to a non-native

624 space, whereas QSM is not. Hence, caution is advised when using QSM in a multi-

625 modal MRI study, and it is strongly recommended to process QSM in its native space

626 prior to any coregistrations.

627

Acknowledgment

634

635

References

637   1.   Hinoda T, Fushimi Y, Okada T, Fujimoto K, Liu C, Yamamoto A, et al.

638   Quantitative Susceptibility Mapping at 3 T and 1.5 T: Evaluation of Consistency and

639   Reproducibility. Invest Radiol. 2015;50(8):522-30. doi:

640   10.1097/RLI.0000000000000159. PubMed PMID: 25900085.

641   2.   Deh K, Nguyen TD, Eskreis-Winkler S, Prince MR, Spincemaille P, Gauthier S, et

642   al. Reproducibility of quantitative susceptibility mapping in the brain at two field

643   strengths from two vendors. Journal of magnetic resonance imaging : JMRI.

644   2015;42(6):1592-600. doi: 10.1002/jmri.24943. PubMed PMID: 25960320; PubMed

645   Central PMCID: PMCPMC4661140.

646   3.   Santin MD, Didier M, Valabregue R, Yahia Cherif L, Garcia-Lorenzo D, Loureiro

647   de Sousa P, et al. Reproducibility of R2 * and quantitative susceptibility mapping (QSM)

648   reconstruction methods in the basal ganglia of healthy subjects. NMR Biomed.

649   2017;30(4). doi: 10.1002/nbm.3491. PubMed PMID: 26913373.

650 4.   Lauzon ML, McCreary CR, McLean DA, Salluzzi M, Frayne R. Quantitative

651 susceptibility mapping at 3 T: comparison of acquisition methodologies. NMR Biomed.

652 2017;30(4). Epub 2016/02/19. doi: 10.1002/nbm.3492. PubMed PMID: 26887659.

653 5.   Lancione M, Tosetti M, Cecchi P, Donatelli G, Cosottini M, Costagli M, editors.

654 Quantitative Susceptibility Mapping at high and ultra-high field: a reproducibility study.

655 Proceedings of International Society for Magnetic Resonance in Medicine; 2018; Paris,

656 France.

657 6.   Rua C, Clarke WT, Driver ID, Mougin O, Clare S, Francis S, et al., editors.

658 Reproducibility of Quantitative Susceptibility Mapping and R2* Mapping of the Human

659 Brain at 7T: a Multi-Centre Pilot Study. Proceedings of International Society for

660 Magnetic Resonance in Medicine; 2018; Paris, France.

661 7.   Okada T, Fujimoto K, Urushibata Y, Kuribayashi H, Kober T, Isa T, editors.

662 Cortical T2* and QSM maps at 7T: test-retest reproducibility, similarity and differences.

663 Proceedings of International Society of Magnetic Resonance in Medicine; 2018; Paris,

664 France.

665 8.   Halchenko YO, Hanke M. Open is Not Enough. Let's Take the Next Step: An

666 Integrated, Community-Driven Computing Platform for Neuroscience. Frontiers in

667 neuroinformatics. 2012;6:22. doi: 10.3389/fninf.2012.00022. PubMed PMID: 23055966;

668 PubMed Central PMCID: PMCPMC3458431.

669 9.   Gorgolewski K, Burns CD, Madison C, Clark D, Halchenko YO, Waskom ML, et

670 al. Nipype: a flexible, lightweight and extensible neuroimaging data processing

671 framework in python. Frontiers in neuroinformatics. 2011;5:13. doi:

672   10.3389/fninf.2011.00013. PubMed PMID: 21897815; PubMed Central PMCID:

673   PMCPMC3159964.

674   10.   Tustison NJ, Avants BB, Cook PA, Zheng YJ, Egan A, Yushkevich PA, et al.

675   N4ITK: Improved N3 Bias Correction. IEEE transactions on medical imaging.

676   2010;29(6):1310-20. doi: 10.1109/Tmi.2010.2046908. PubMed PMID:

677   WOS:000278535800009.

678   11.   Jenkinson M, Smith S. A global optimisation method for robust affine registration

679   of brain images. Medical image analysis. 2001;5(2):143-56. doi: Doi 10.1016/S1361-

680   8415(01)00036-6. PubMed PMID: WOS:000169672400005.

681   12.   Jenkinson M, Bannister P, Brady M, Smith S. Improved optimization for the

682   robust and accurate linear registration and motion correction of brain images.

683   NeuroImage. 2002;17(2):825-41. doi: 10.1006/nimg.2002.1132. PubMed PMID:

684   WOS:000178642000027.

685   13.   Miller AJ, Joseph PM. The Use of Power Images to Perform Quantitative-

686   Analysis on Low Snr Mr-Images. Magnetic resonance imaging. 1993;11(7):1051-6. doi:

687   Doi 10.1016/0730-725x(93)90225-3. PubMed PMID: WOS:A1993MB03400017.

688   14.   Reichenbach JR, Schweser F, Serres B, Deistung A. Quantitative Susceptibility

689   Mapping: Concepts and Applications. Clin Neuroradiol. 2015;25:225-30. doi:

690   10.1007/s00062-015-0432-9. PubMed PMID: WOS:000361820200026.

691   15.   Wharton S, Bowtell R. Fiber orientation-dependent white matter contrast in

692   gradient echo MRI. Proceedings of the National Academy of Sciences of the United

693   States of America. 2012;109(45):18559-64. doi: 10.1073/pnas.1211075109. PubMed

694   PMID: WOS:000311156700069.

695   16.   Sati P, van Gelderen P, Silva AC, Reich DS, Merkle H, de Zwart JA, et al. Micro-

696   compartment specific T*(2) relaxation in the brain. NeuroImage. 2013;77:268-78. doi:

697   10.1016/j.neuroimage.2013.03.005. PubMed PMID: WOS:000320073900027.

698   17.   Li W, Wu B, Liu C. Quantitative susceptibility mapping of human brain reflects

699   spatial variation in tissue composition. NeuroImage. 2011;55(4):1645-56. doi:

700   10.1016/j.neuroimage.2010.11.088. PubMed PMID: 21224002; PubMed Central

701   PMCID: PMCPMC3062654.

702   18.   Schweser F, Deistung A, Lehr BW, Reichenbach JR. Quantitative imaging of

703   intrinsic magnetic tissue properties using MRI signal phase: An approach to in vivo brain

704   iron metabolism? NeuroImage. 2011;54(4):2789-807. doi:

705   10.1016/j.neuroimage.2010.10.070. PubMed PMID: WOS:000286495800024.

706   19.   Wu B, Li W, Guidon A, Liu CL. Whole brain susceptibility mapping using

707   compressed sensing. Magnet Reson Med. 2012;67(1):137-47. doi: 10.1002/mrm.23000.

708   PubMed PMID: WOS:000298482800016.

709   20.   Li W, Avram AV, Wu B, Xiao X, Liu CL. Integrated Laplacian-based phase

710   unwrapping and background phase removal for quantitative susceptibility mapping. Nmr

711   in Biomedicine. 2014;27(2):219-27. doi: 10.1002/nbm.3056. PubMed PMID:

712   WOS:000329986900012.

713   21.   Bao L, Li X, Cai C, Chen Z, van Zijl PC. Quantitative Susceptibility Mapping

714   Using Structural Feature Based Collaborative Reconstruction (SFCR) in the Human

715   Brain. IEEE transactions on medical imaging. 2016;35(9):2040-50. doi:

716   10.1109/TMI.2016.2544958. PubMed PMID: 27019480; PubMed Central PMCID:

717   PMCPMC5495149.

718   22.   Jenkinson M, Beckmann CF, Behrens TE, Woolrich MW, Smith SM. Fsl.

719   NeuroImage. 2012;62(2):782-90. doi: 10.1016/j.neuroimage.2011.09.015. PubMed

720   PMID: WOS:000306390600032.

721   23.   Elkady AM, Sun H, Wilman AH. Importance of extended spatial coverage for

722   quantitative susceptibility mapping of iron-rich deep gray matter. Magnetic resonance

723   imaging. 2016;34(4):574-8. doi: 10.1016/j.mri.2015.12.032. PubMed PMID: 26721523.

724   24.   Haacke EM, Liu S, Buch S, Zheng W, Wu D, Ye Y. Quantitative susceptibility

725   mapping: current status and future directions. Magnetic resonance imaging.

726   2015;33(1):1-25. doi: 10.1016/j.mri.2014.09.004. PubMed PMID: 25267705.

727   25.   Liu C, Wei H, Gong NJ, Cronin M, Dibb R, Decker K. Quantitative Susceptibility

728   Mapping: Contrast Mechanisms and Clinical Applications. Tomography. 2015;1(1):3-17.

729   doi: 10.18383/j.tom.2015.00136. PubMed PMID: 26844301; PubMed Central PMCID:

730   PMCPMC4734903.

731   26.   Schweser F, Deistung A, Reichenbach JR. Foundations of MRI phase imaging

732   and processing for Quantitative Susceptibility Mapping (QSM). Z Med Phys.

733   2016;26(1):6-34. doi: 10.1016/j.zemedi.2015.10.002. PubMed PMID: 26702760.

734   27.   Langkammer C, Bredies K, Poser BA, Barth M, Reishofer G, Fan AP, et al. Fast

735   quantitative susceptibility mapping using 3D EPI and total generalized variation.

736   NeuroImage. 2015;111:622-30. Epub 2015/03/04. doi:

737   10.1016/j.neuroimage.2015.02.041. PubMed PMID: 25731991.

738   28.   Liu Z, Kee Y, Zhou D, Wang Y, Spincemaille P. Preconditioned total field

739   inversion (TFI) method for quantitative susceptibility mapping. Magn Reson Med.

740   2017;78(1):303-15. Epub 2016/07/29. doi: 10.1002/mrm.26331. PubMed PMID:

741   27464893; PubMed Central PMCID: PMCPMC5274595.

742   29.   Chatnuntawech I, McDaniel P, Cauley SF, Gagoski BA, Langkammer C, Martin

743   A, et al. Single-step quantitative susceptibility mapping with variational penalties. NMR

744   Biomed. 2017;30(4). Epub 2016/06/23. doi: 10.1002/nbm.3570. PubMed PMID:

745   27332141; PubMed Central PMCID: PMCPMC5179325.

746   30.   Wang Y, Liu T. Quantitative susceptibility mapping (QSM): Decoding MRI data

747   for a tissue magnetic biomarker. Magn Reson Med. 2015;73(1):82-101. doi:

748   10.1002/mrm.25358. PubMed PMID: 25044035; PubMed Central PMCID:

749   PMCPMC4297605.

750   31.   Deistung A, Schweser F, Reichenbach JR. Overview of quantitative susceptibility

751   mapping. NMR Biomed. 2017;30(4). doi: 10.1002/nbm.3569. PubMed PMID: 27434134.

752   32.   Liu T, Spincemaille P, de Rochefort L, Kressler B, Wang Y. Calculation of

753   susceptibility through multiple orientation sampling (COSMOS): a method for

754   conditioning the inverse problem from measured magnetic field map to susceptibility

755   source image in MRI. Magn Reson Med. 2009;61(1):196-204. doi: 10.1002/mrm.21828.

756   PubMed PMID: 19097205.

757   33.   Bilgic B, Pfefferbaum A, Rohlfing T, Sullivan EV, Adalsteinsson E. MRI estimates

758   of brain iron concentration in normal aging using quantitative susceptibility mapping.

759   NeuroImage. 2012;59(3):2625-35. doi: 10.1016/j.neuroimage.2011.08.077. PubMed

760   PMID: 21925274; PubMed Central PMCID: PMCPMC3254708.

761   34.   Li X, Harrison DM, Liu H, Jones CK, Oh J, Calabresi PA, et al. Magnetic

762   susceptibility contrast variations in multiple sclerosis lesions. Journal of magnetic

35

763   resonance imaging : JMRI. 2016;43(2):463-73. doi: 10.1002/jmri.24976. PubMed PMID:

764   26073973; PubMed Central PMCID: PMCPMC4678033.

765   35.   Deistung A, Schafer A, Schweser F, Biedermann U, Turner R, Reichenbach JR.

766   Toward in vivo histology: a comparison of quantitative susceptibility mapping (QSM)

767   with magnitude-, phase-, and R2*-imaging at ultra-high magnetic field strength.

768   NeuroImage. 2013;65:299-314. doi: 10.1016/j.neuroimage.2012.09.055. PubMed PMID:

769   23036448.

770   36.   Schmalbrock P, Prakash RS, Schirda B, Janssen A, Yang GK, Russell M, et al.

771   Basal Ganglia Iron in Patients with Multiple Sclerosis Measured with 7T Quantitative

772   Susceptibility Mapping Correlates with Inhibitory Control. AJNR American journal of

773   neuroradiology. 2016;37(3):439-46. doi: 10.3174/ajnr.A4599. PubMed PMID: 26611996.

774   37.   Straub S, Schneider TM, Emmerich J, Freitag MT, Ziener CH, Schlemmer HP, et

775   al. Suitable reference tissues for quantitative susceptibility mapping of the brain. Magn

776   Reson Med. 2016. doi: 10.1002/mrm.26369. PubMed PMID: 27529579.

777
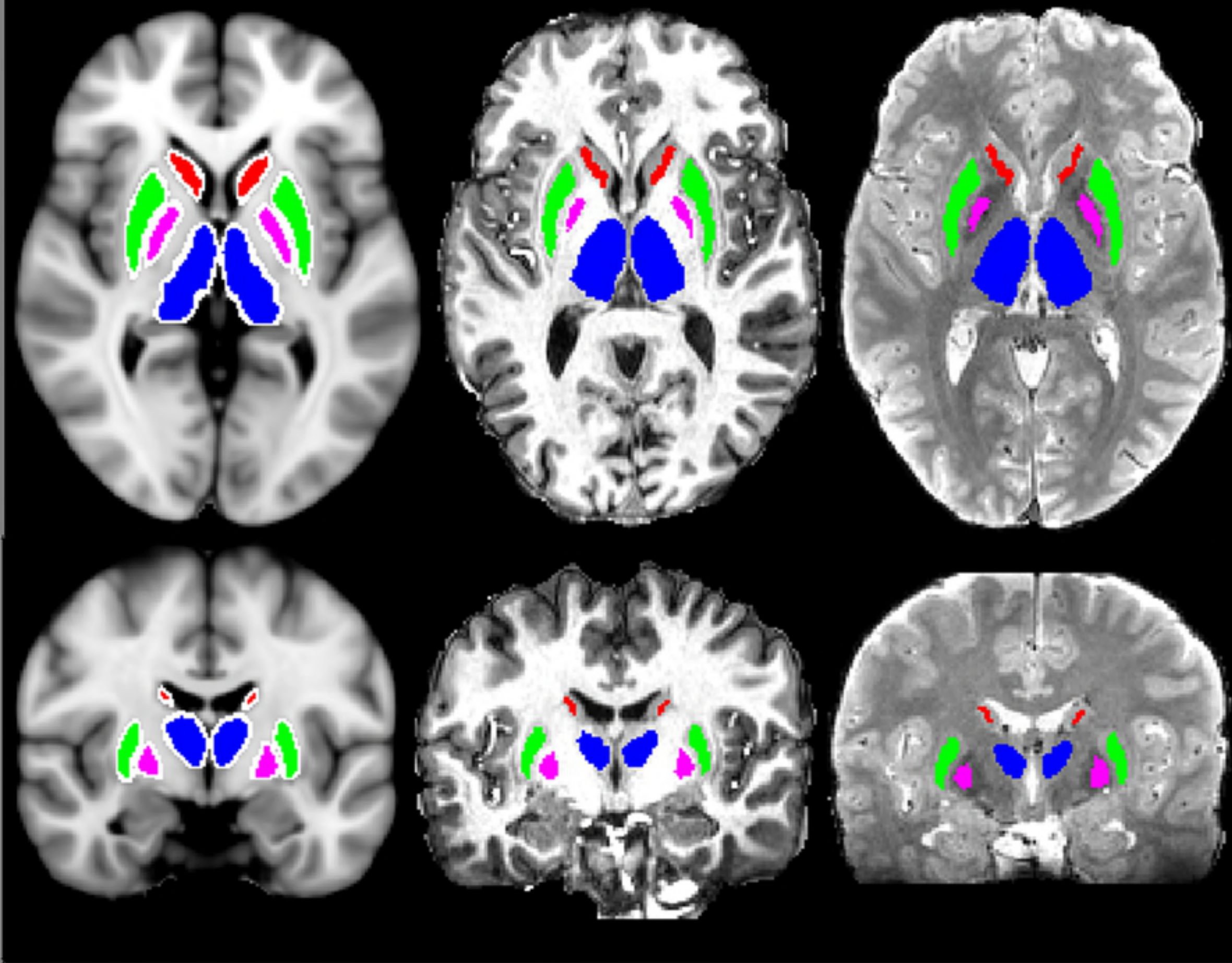
Fig1
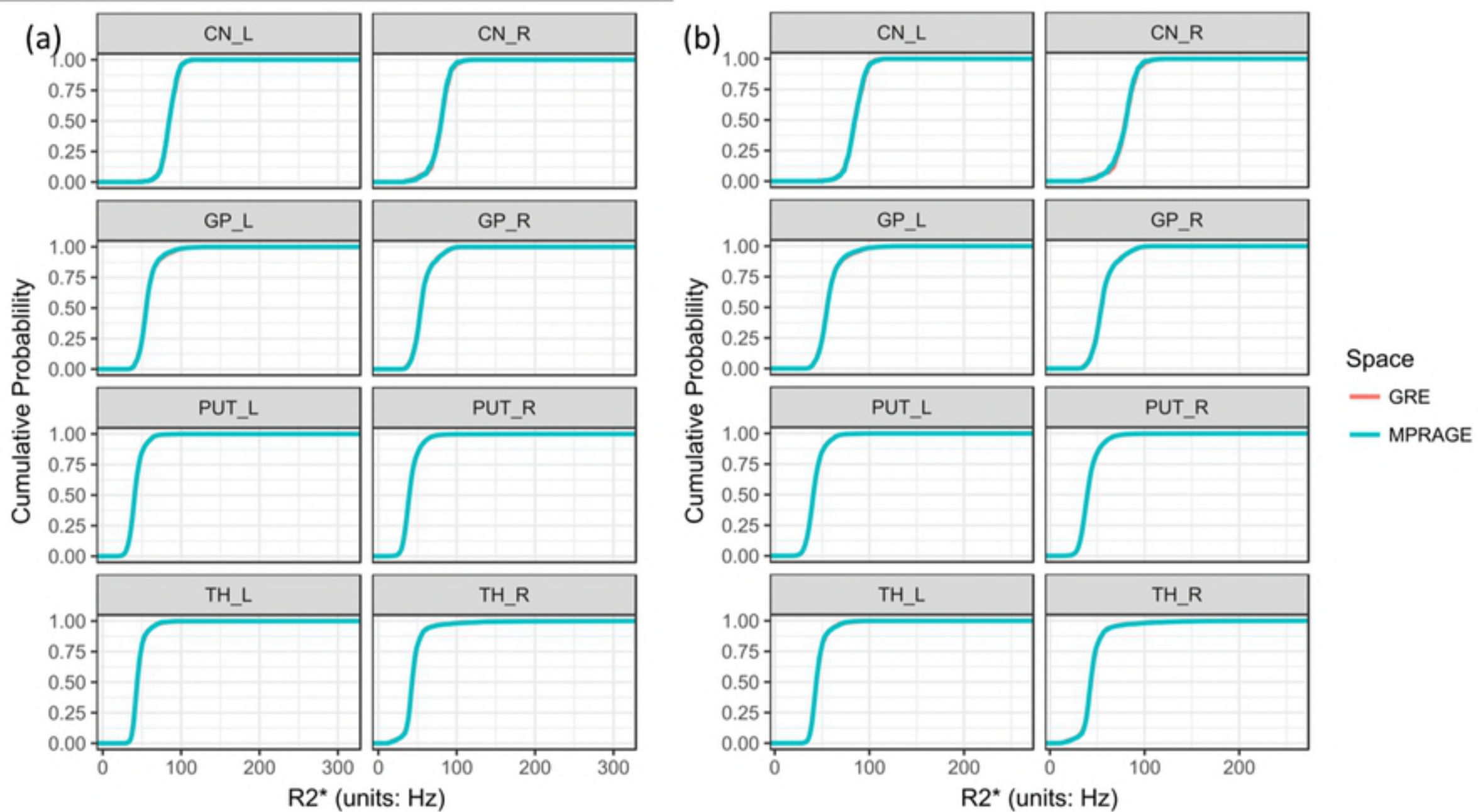
Fig2
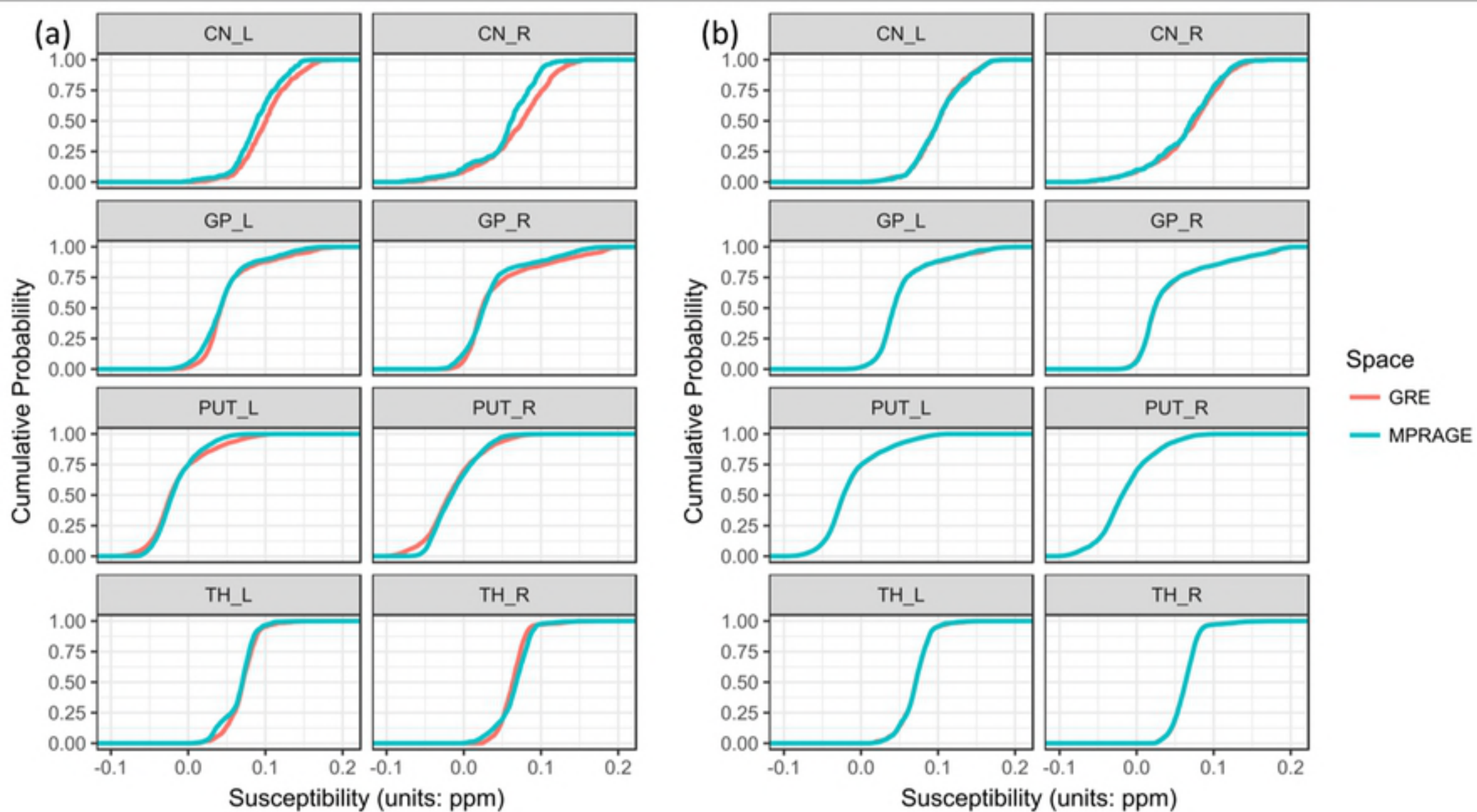
Fig3
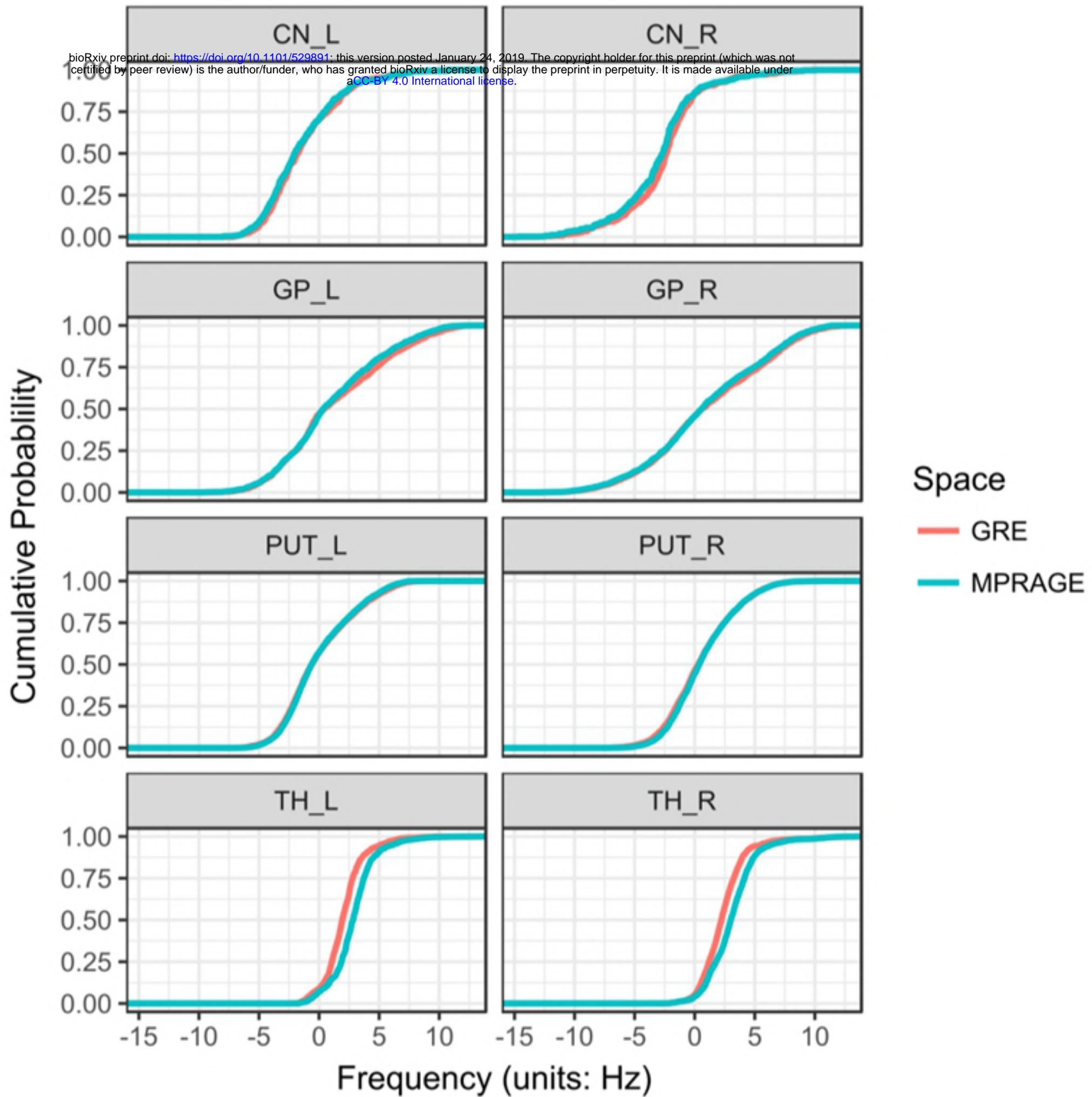
Fig4

(a) Source GRE Coregistration
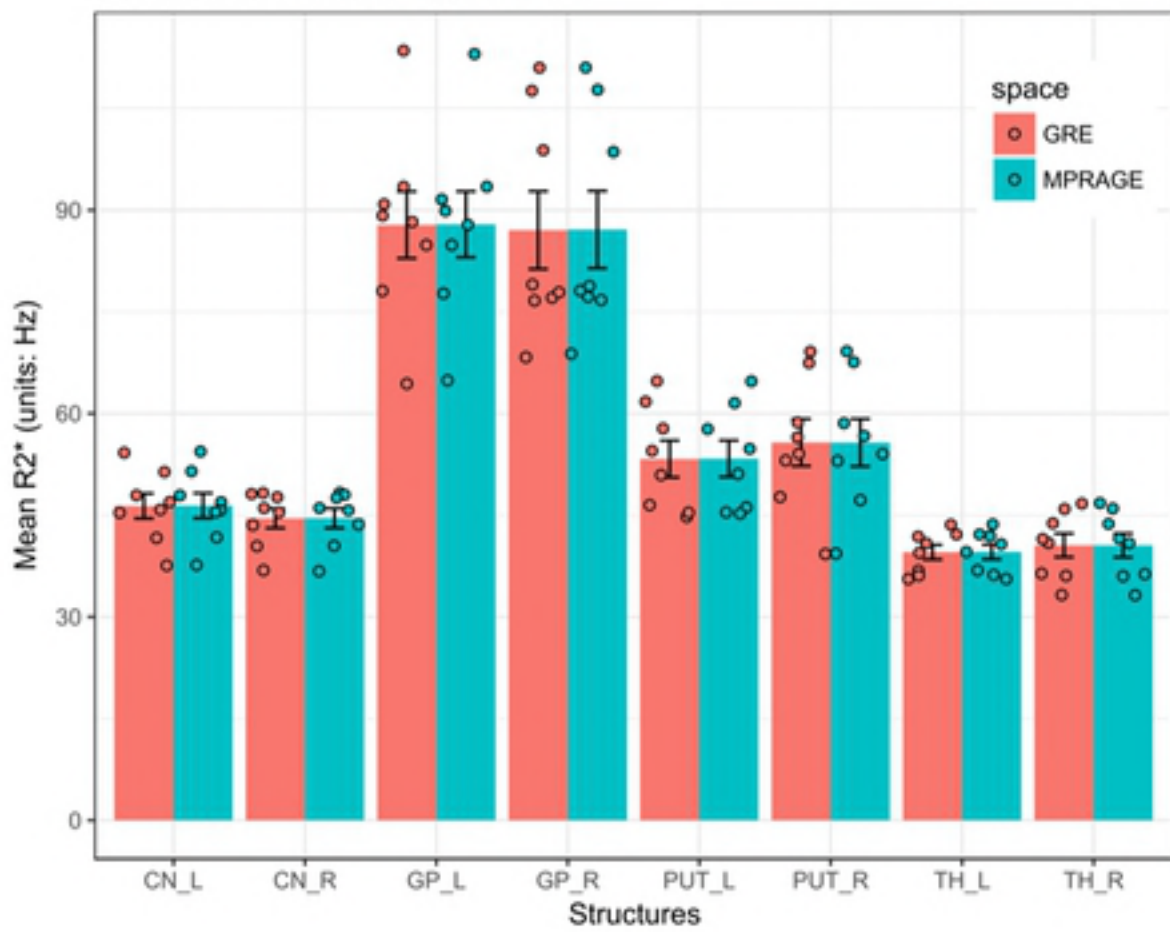
(b) Direct R2* map Coregistration
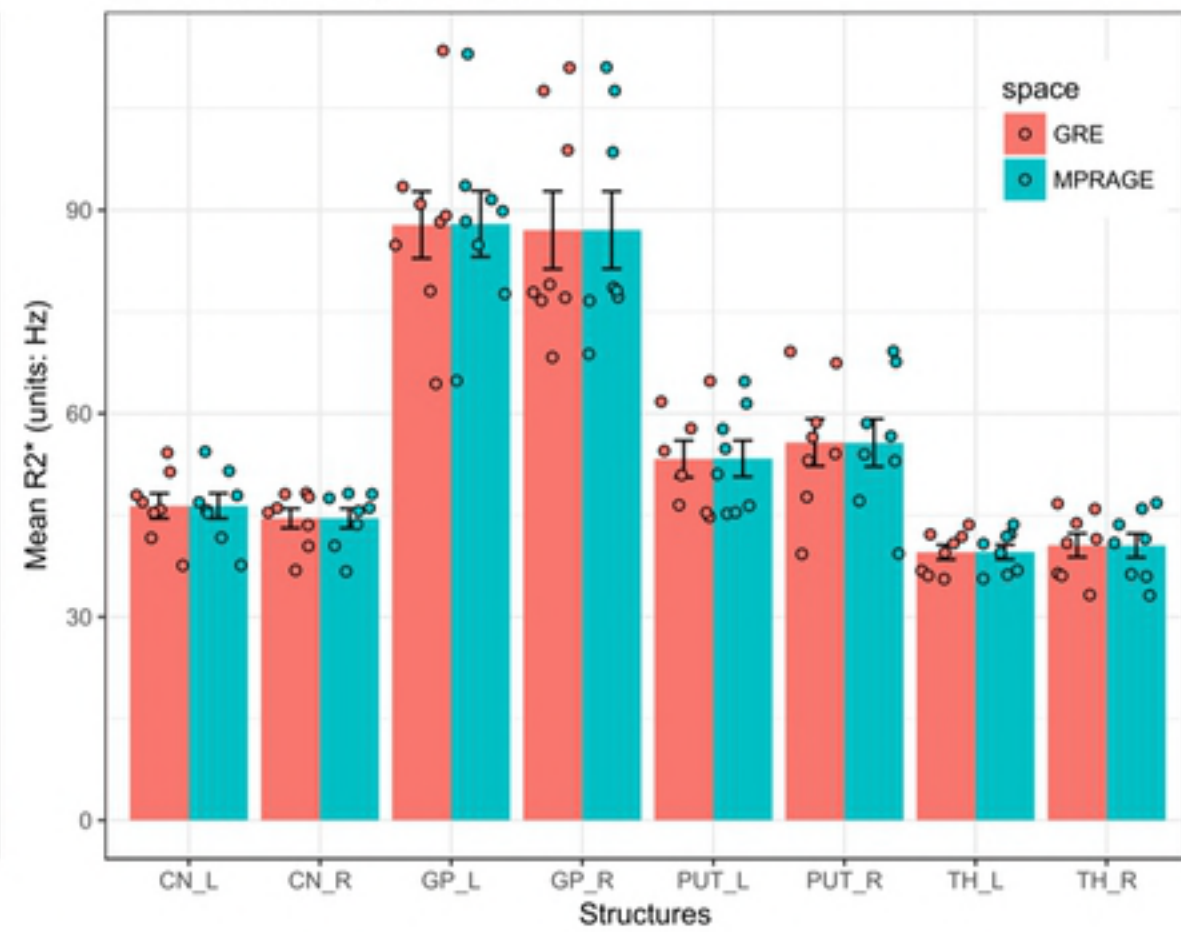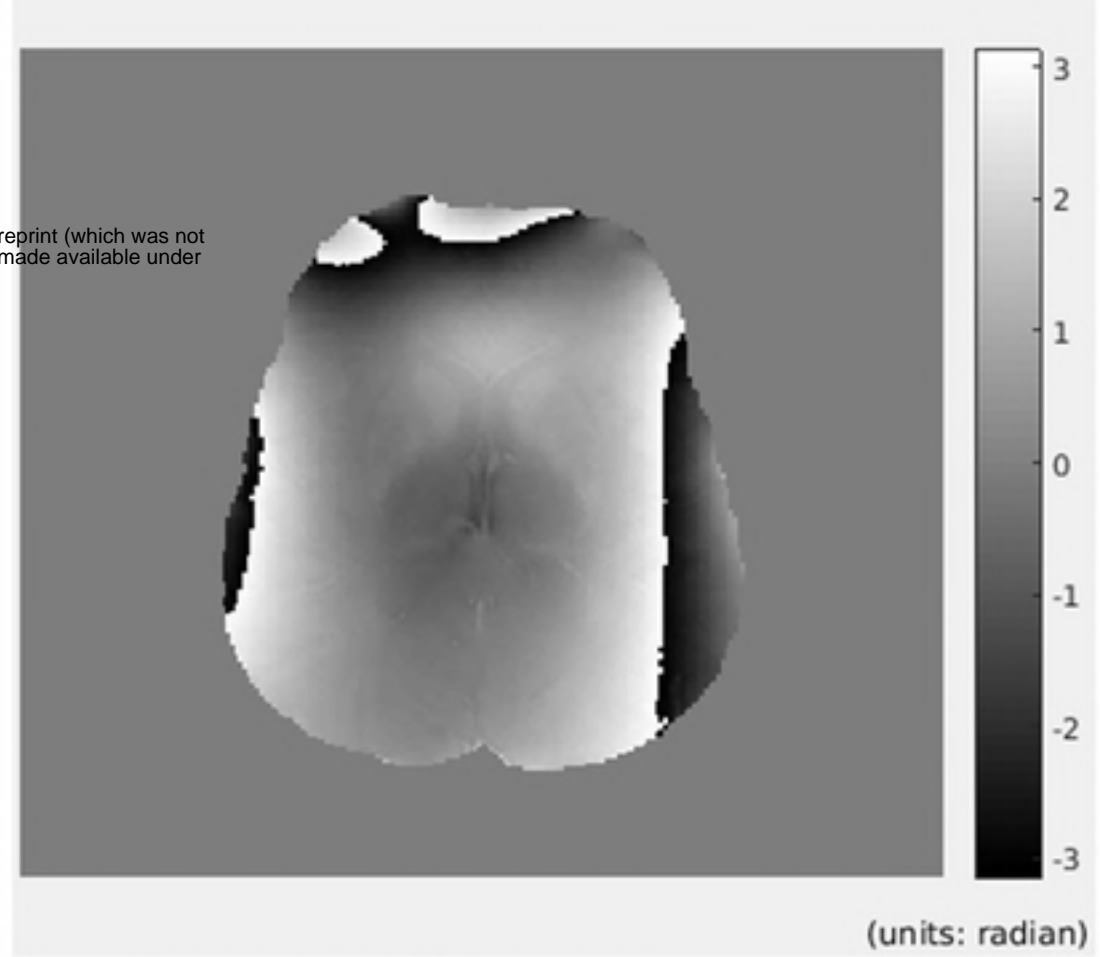
Fig5
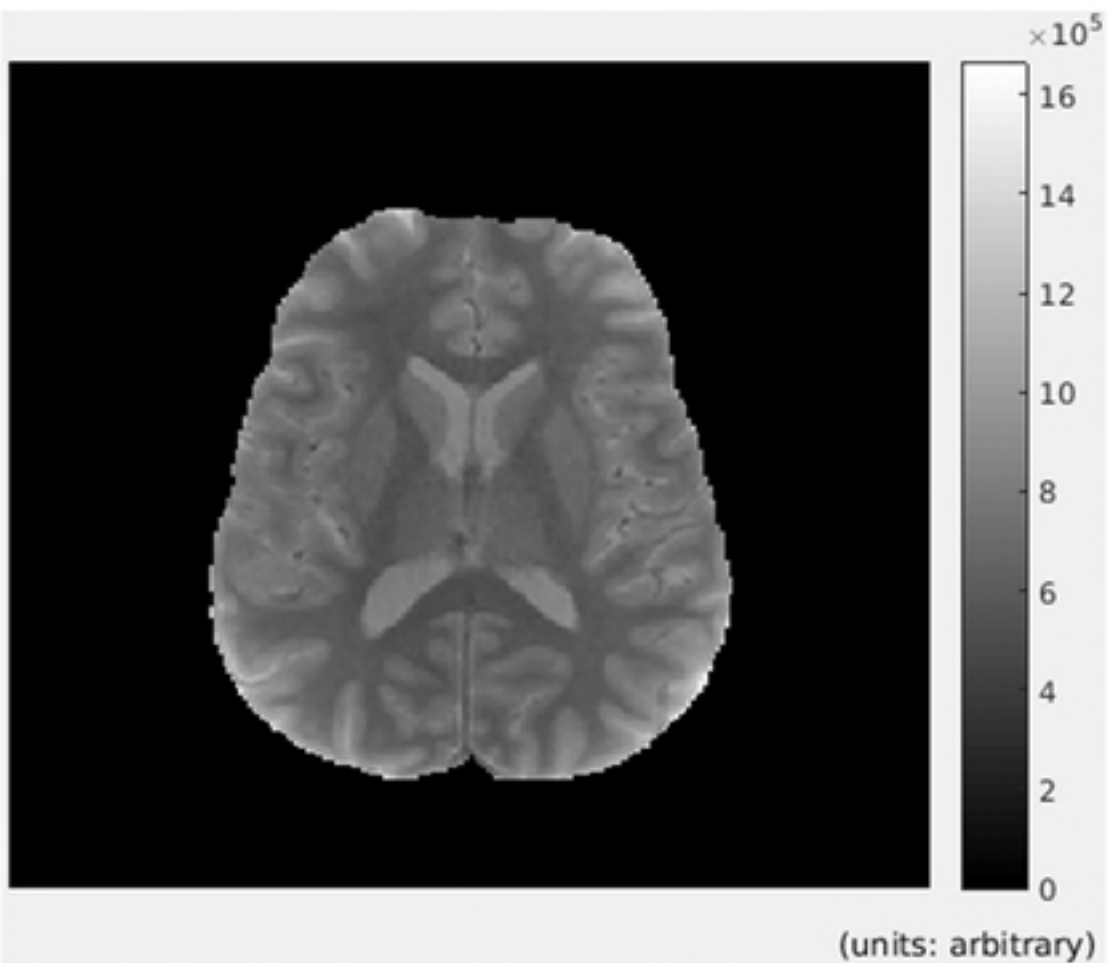
(a) Source GRE Coregistration
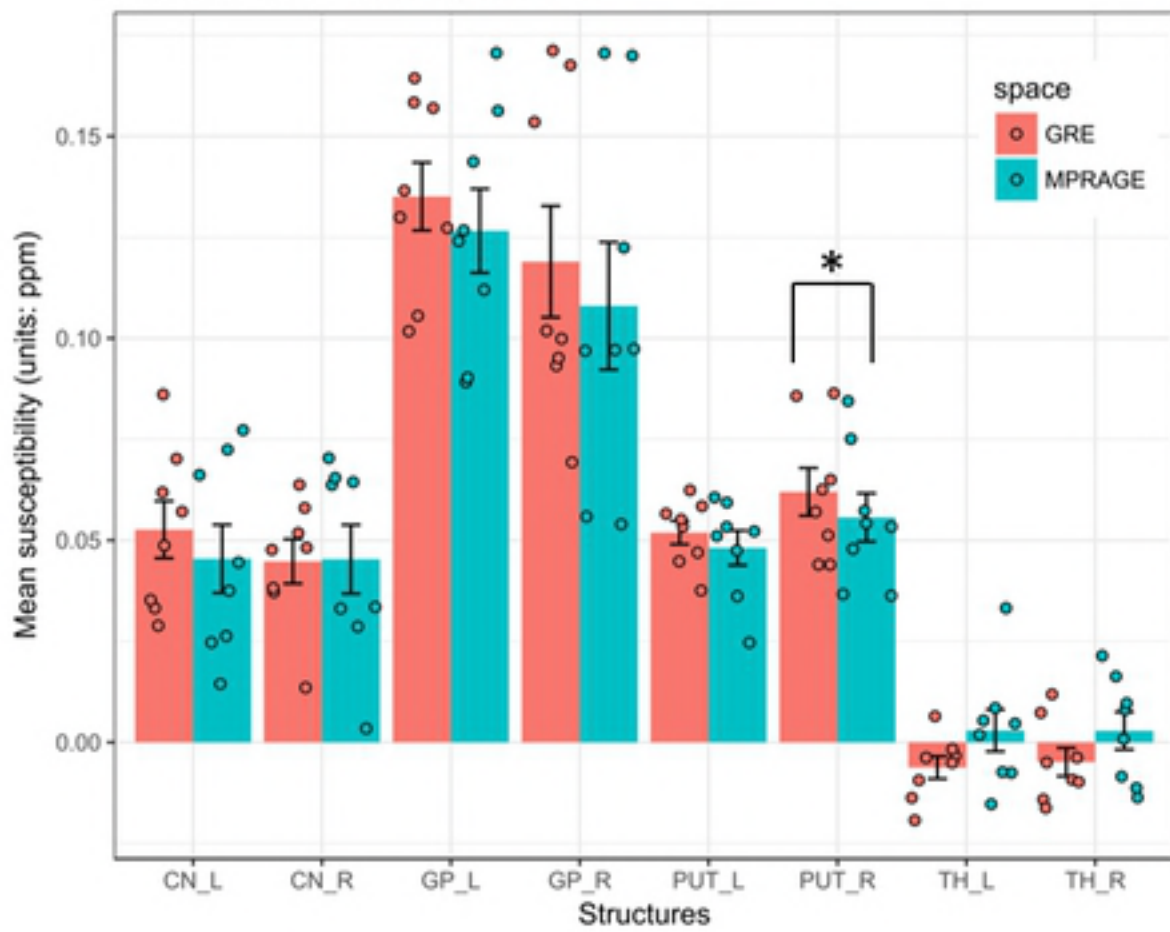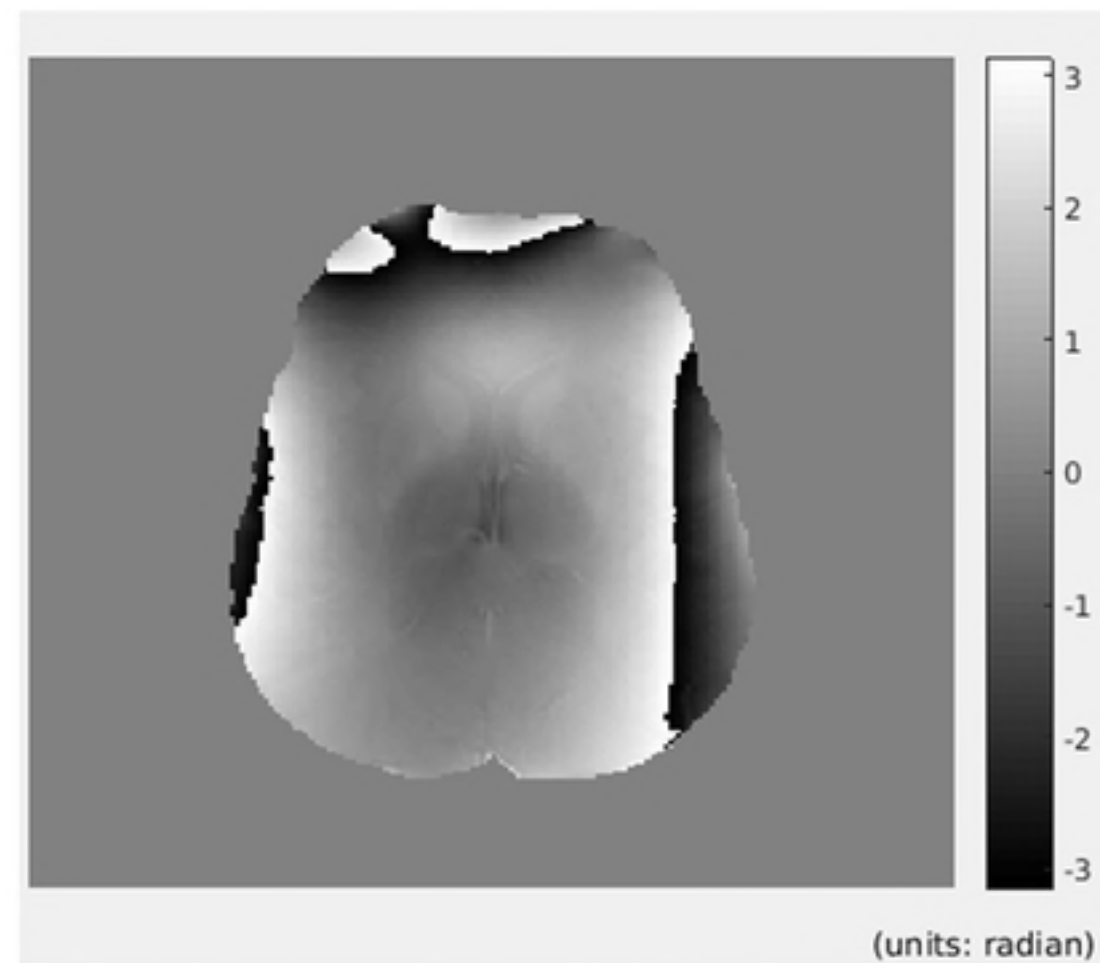
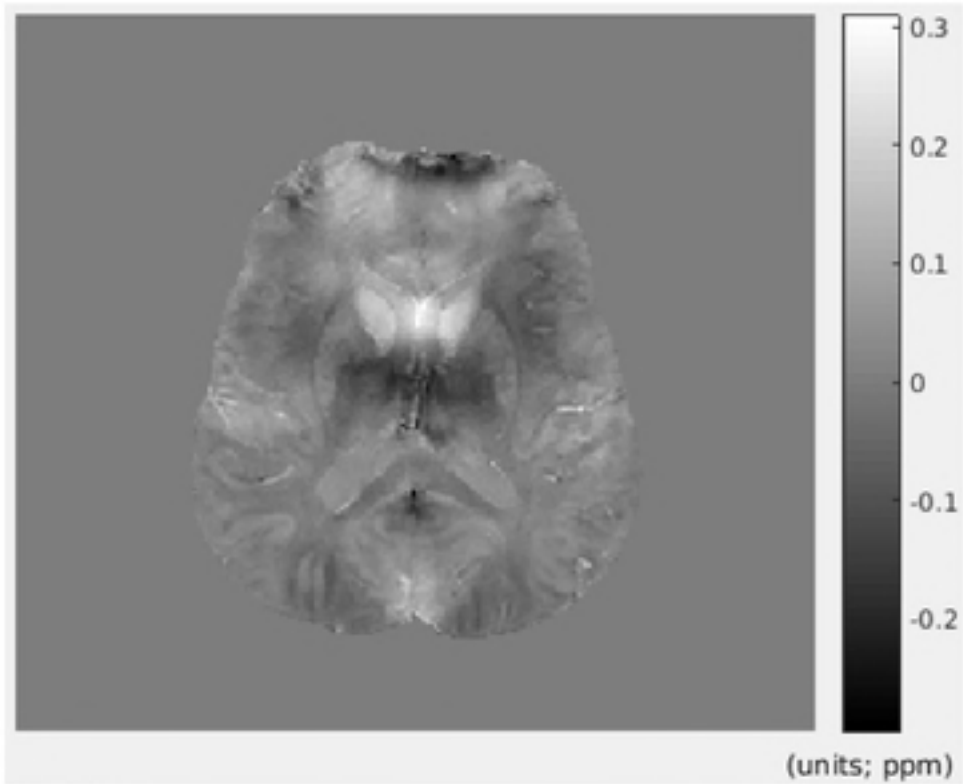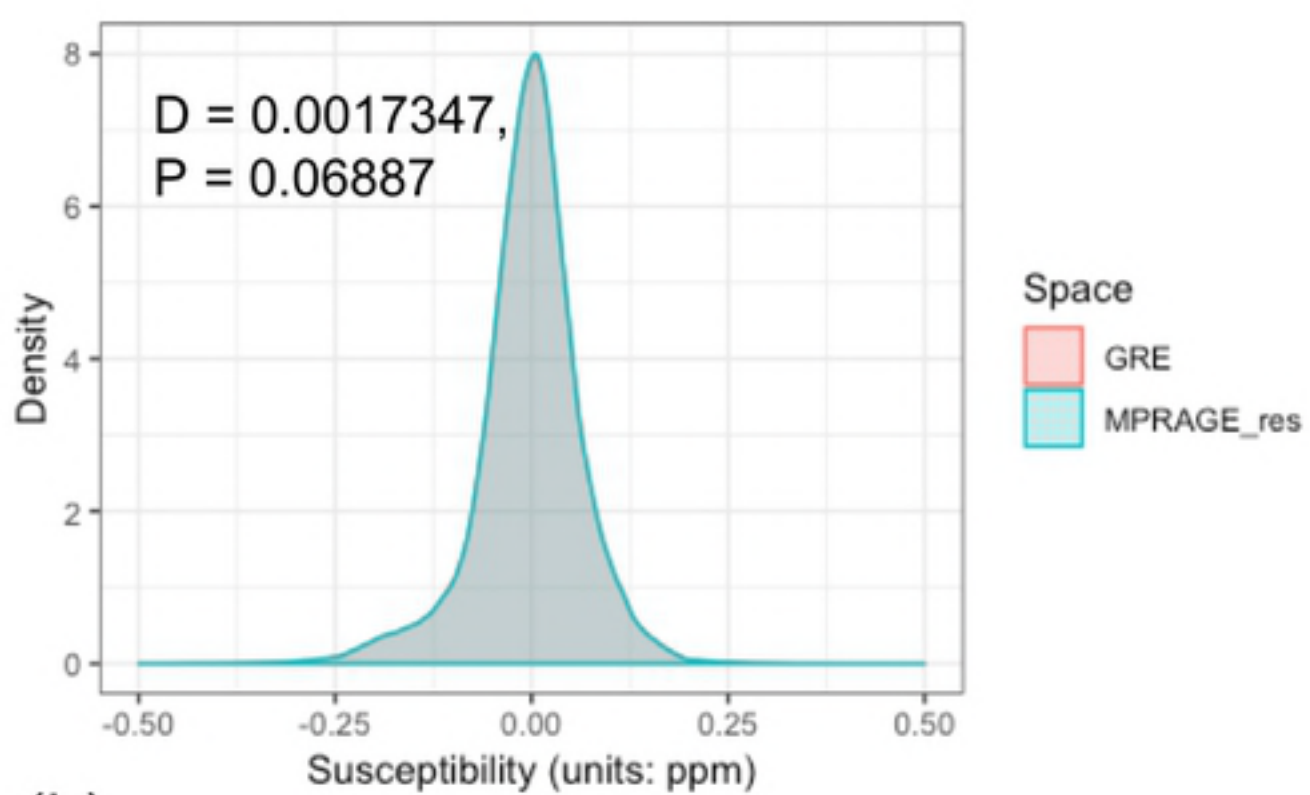**(b) Direct QSM Coregistration**
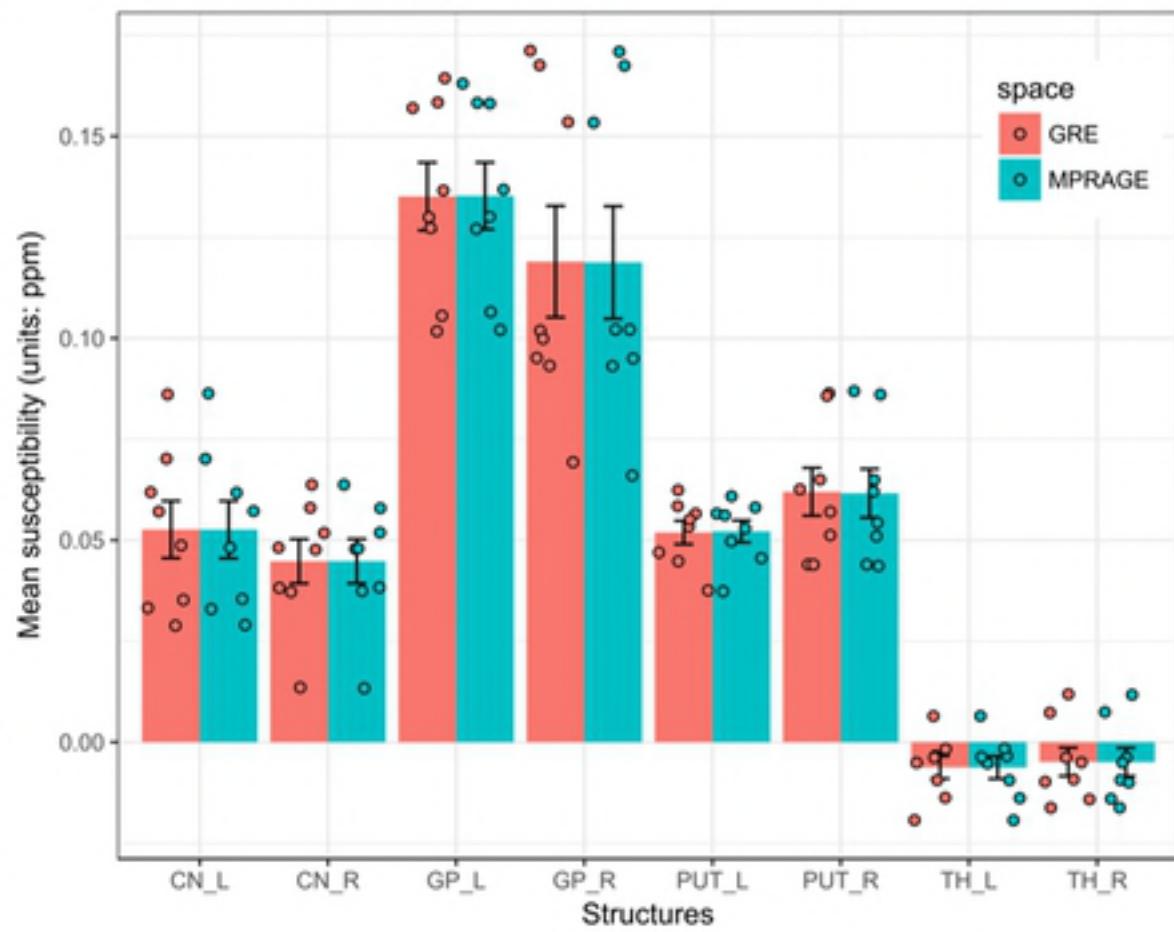
Fig6
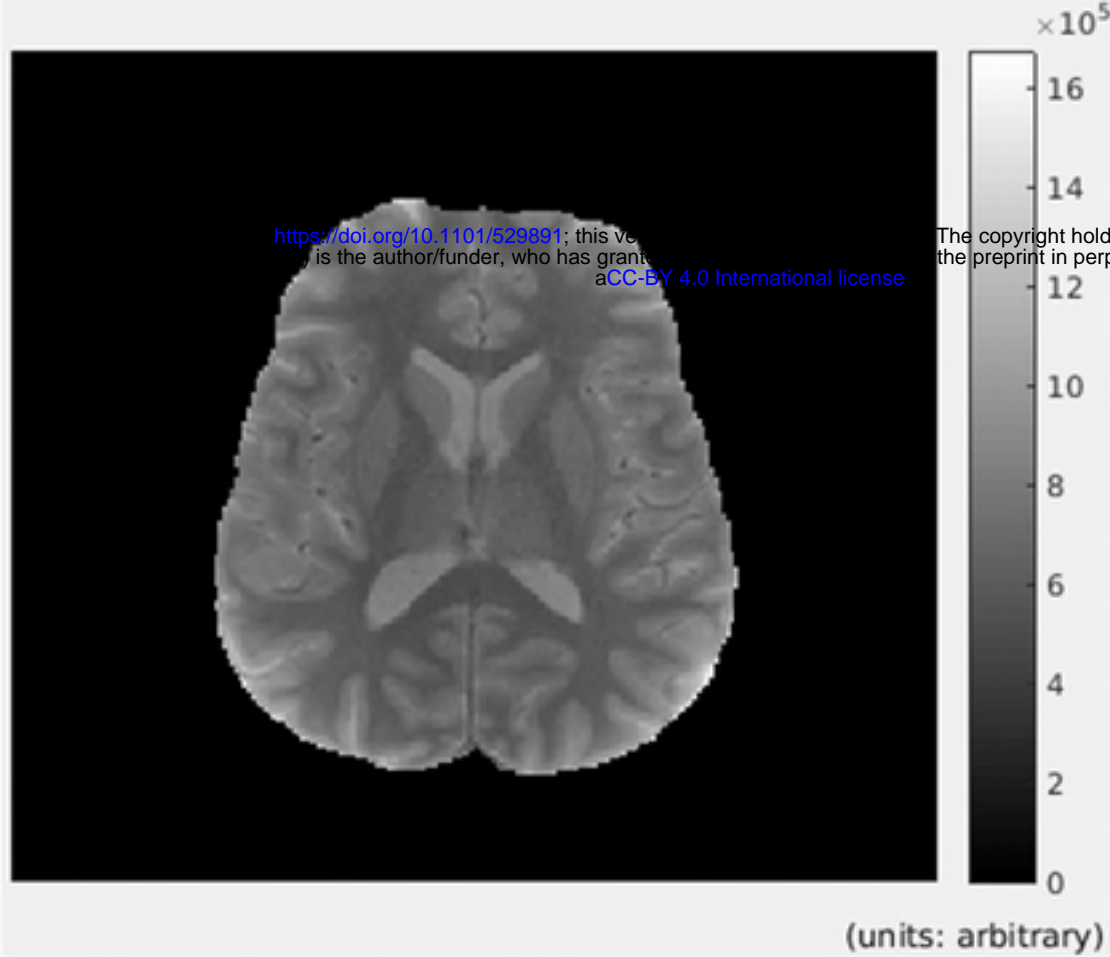
(a) Magnitude in GRE space

(b) Phase in GRE space

(c) Magnitude in interpolated GRE space

(d) Phase in interpolated GRE space

Fig7

Fig8
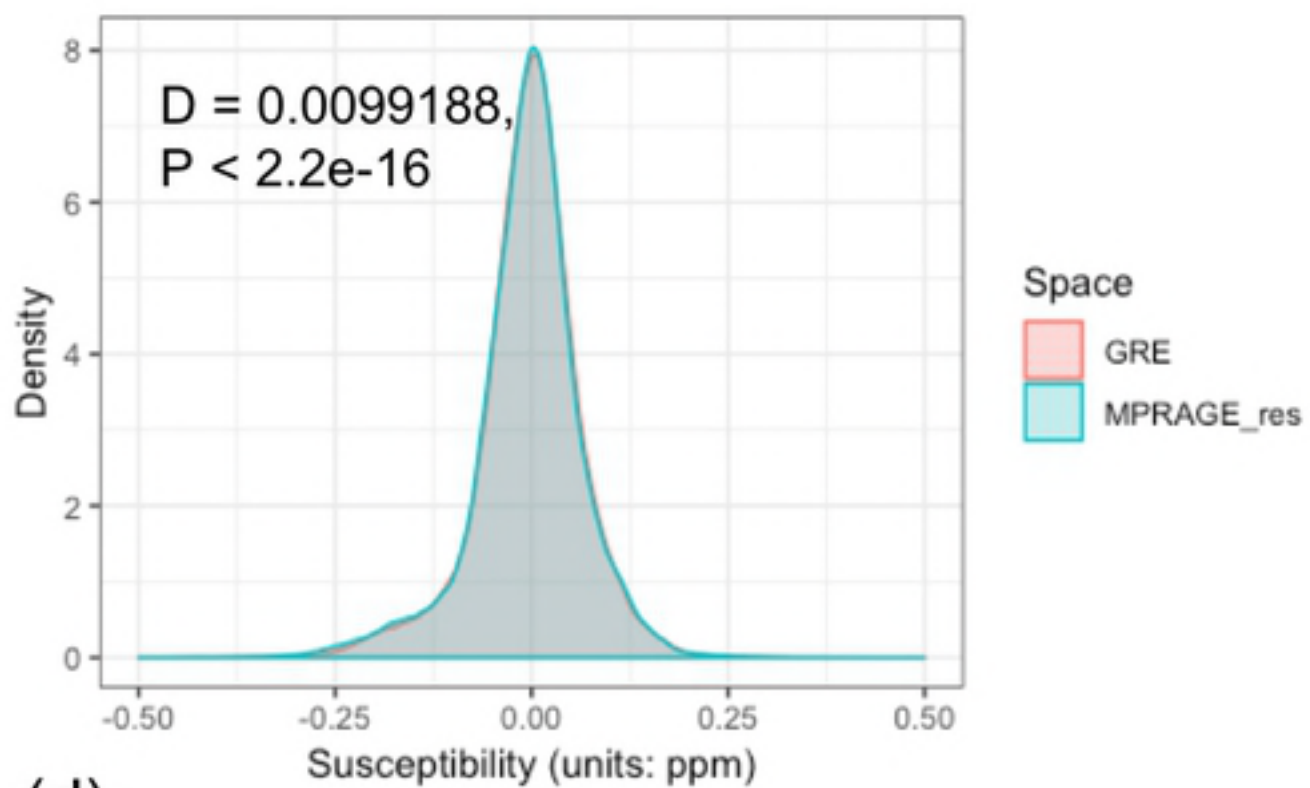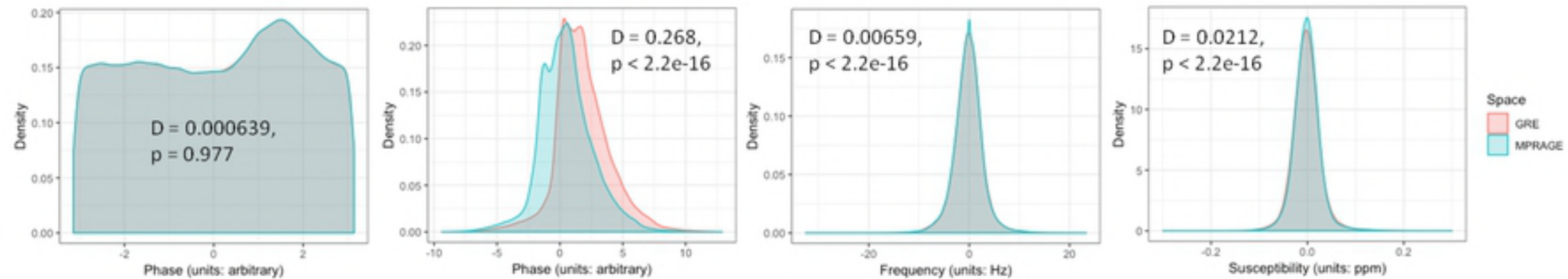
(a) Raw phase   (b) Unwrapped phase   (c) Frequency map   (d) QSM

Fig9